DOI: https://doi.org/10.2138/am-2021-7825. http://www.minsocam.org/

Revision 2 (Clean)

Oxygen isotope evidence for input of magmatic fluids and precipitation of Au-Ag-tellurides in an otherwise ordinary adularia-sericite epithermal system in NE China

Shen Gao[1, 2*] (***Corresponding Author***), Albert H. Hofstra[3], Xinyu Zou[1, 2], John W. Valley[4], Kouki Kitajima[4], Erin E. Marsh[3], Heather A. Lowers[3], David T. Adams[3], Kezhang Qin[1, 2, 5], Hong Xu[6]

[1] *Key Laboratory of Mineral Resources, Institute of Geology and Geophysics, Chinese Academy of Sciences, Beijing 100029, China*

[2] *Innovation Academy for Earth Science, Chinese Academy of Sciences, Beijing 100029, China*

[3] *U.S. Geological Survey, P.O. Box 25046, Denver, CO 80225, USA*

[4] *WiscSIMS, Department of Geoscience, University of Wisconsin-Madison, 1215 West Dayton Street, Madison, WI 53706, USA*

[5] *University of Chinese Academy of Sciences, Beijing 100049, China*

[6] *School of Earth Sciences and Resources, China University of Geosciences (Beijing), Beijing 100083, China*

Submitted to: **American Mineralogist**

Submission date: **12/21/2020**

Abstract

Tellurium (Te)-rich adularia-sericite epithermal Au-Ag deposits are an important current and future source of precious and critical metals. However, the source and evolution of ore-forming fluids in these deposits are masked by traditional bulk analysis of quartz oxygen isotope ratios that homogenize fine scale textures and growth zones. To advance understanding of the source of Te and precious metals, herein, we use petrographic and cathodoluminescence (CL) images of such textures and growth zones to guide high spatial resolution secondary ion mass spectroscopy (SIMS) oxygen isotope analyses (10-μm spot) and spatially correlated fluid inclusion microthermometric measurements on successive quartz bands in contemporary Te-rich and Te-poor adularia-sericite (-quartz) epithermal Au-Ag vein deposits in northeastern China. The results show that large positive oxygen isotope shifts from -7.1 to +7.7‰ in quartz rims are followed by precipitation of Au-Ag telluride minerals in the Te-rich deposit, whereas small oxygen isotope shifts of only 4‰ (-2.2 to +1.6‰) were detected in quartz associated with Au-Ag minerals in the Te-poor deposits. Moreover, fluid-inclusion homogenization temperatures are higher in comb quartz rims (avg. 266.4 to 277.5 °C) followed by Au-Ag telluride minerals than in previous stages (~250 °C) in the Te-rich deposit. The Te-poor deposit has a consistent temperature (~245 °C) in quartz that pre- and postdates Au-Ag minerals. Together, the coupled increase in oxygen isotope ratios and homogenization temperatures followed by precipitation of Au-Ag tellurides strongly

supports that inputs of magmatic fluid containing Au, Ag, and Te into barren meteoric water-dominated flow systems are critical to formation of Te-rich adularia-sericite epithermal Au-Ag deposits. In contrast, Te-poor adularia-sericite epithermal Au-Ag deposits show little or no oxygen isotope or fluid inclusion evidence for inputs of magmatic fluid.

Key words: quartz, SIMS, oxygen isotopes, fluid inclusions, magmatic fluid, Te, epithermal Au-Ag deposits

1. Introduction

Tellurium (Te)-rich adularia-sericite epithermal Au-Ag deposits are important producers of gold throughout the world (Ahmad et al. 1987; Spry et al. 1996; Cooke and McPhail 2001; Cook and Ciobanu 2005; Ciobanu et al. 2006; Voudouris 2006; Cook et al. 2009; Saunders and Brueseke 2012; Goldfarb et al. 2016, 2017; Kelley and Spry 2016; Zhai et al. 2018; Keith et al. 2020). Some of these deposits are associated with alkalic volcano-plutonic centers (e.g., Cripple Creek; Kelley et al. 1998) and others with calc-alkalic volcano-plutonic centers (e.g., Sandaowanzi; Gao et al. 2017). Furthermore, the magmatic belts that contain Te-rich Au-Ag deposits can also host Te-poor Au-Ag deposits (e.g., Dong'an; Zhang et al. 2010a and reference therein). The source of Te in continental magmatic belts has been attributed to the nature of sub continental lithospheric mantle (SCLM) (e.g., Holwell et al. 2019). These deposits are economically important and are a potential source of Te, which is a critical commodity for modern technology, if current metallurgical impediments are resolved (Spry et al. 2004; Ciobanu et al. 2006; Cook et al. 2009; Goldfarb et al. 2016, 2017; Kelley and Spry 2016; Jenkin et al. 2019).

In magmatic-hydrothermal systems, Te is generally interpreted to be derived from igneous intrusions (Jensen and Barton 2000; Saunders and Brueseke 2012; Kelley and Spry 2016; Holwell et al. 2019); thus, magmatic fluids have been proposed to be involved in the formation of Te-rich epithermal Au-Ag deposits (e.g., Ciobanu et al. 2006). Recently, high-precision in situ oxygen isotope analyses by ion microprobe are regarded to be the most effective way to detect short-lived oxygen isotope variations, which can record transient variations of fluid inputs in hydrothermal ore deposits (Valley and Graham, 1996; Smith et al. 1998; Valley et al., 1998; Saunders et al., 2008; Tanner et al., 2013; Fekete et al., 2016; Cernuschi et al., 2018; Li et al., 2019; Haroldson et al., 2020). However, in situ isotopic evidence in Te-rich epithermal Au-Ag deposits is scarce; thus, the role of magmatic fluids in Te-rich epithermal Au-Ag deposits is still unclear. The large range of oxygen isotope values in quartz obtained by conventional technique from Te-rich epithermal deposits allows several interpretations. The highest $\delta^{18}O(Qz)$ values of up to 20‰ (e.g., Cripple Creek, Colorado, USA; Beaty 1996) are indicative of a magmatic fluid dominated system (e.g., Taylor 1997; Hedenquist et al. 1998). In contrast, many other deposits have lower $\delta^{18}O(Qz)$ values close to 0‰, such as Tongyoung (Korea) ~3‰ (Shelton et al. 1990) and Sandaowanzi (northeast China) from -3.9 to -0.2‰ (Wu et al., 2005a; Zhai et al. 2018) that are indicative of meteoric water dominated systems (O'Neil and Silberman 1974; Hedenquist and Lowenstern 1994; Simmons 1995; John et al. 2003; Simmons et al. 2005). The low oxygen isotope values raise the question: Is magmatic fluid needed to form a Te-rich Au-Ag deposit? If needed, what process causes Au-Ag telluride minerals to precipitate from magmatic fluids in epithermal systems (e.g., fluid boiling, mixing of magmatic fluid with meteoric water, or cooling; Anderson and Eaton 1990; Cooke and McPhail 2001; Zhai et al. 2018)? How do ore-forming processes differ between Te-rich and Te-poor epithermal Au-Ag deposits with low oxygen isotope values (e.g., $\delta^{18}O(Qz)$ = 7-9‰ at Hishikari, Japan; $\delta^{18}O(Qz)$ = -3.0 to 1.5‰ at Dong'an, northeastern China; Faure et al. 2002; Han 2013)?

To investigate these questions, we studied the contemporary Te-rich Sandaowanzi and Te-poor Dong'an adularia-sericite epithermal Au-Ag deposits situated in an Early Cretaceous continental magmatic arc in northeastern China. We used mineral textures and cathodoluminescence (CL) imaging to guide high spatial resolution secondary ion mass spectroscopy (SIMS) oxygen isotope analyses in combination with fluid inclusion microthermometric measurements of the same generation of quartz to advance understanding of the source and evolution of hydrothermal fluids in these two deposits. The results show a large difference in the oxygen isotope ratios of quartz is associated with Te-rich vs. Te-poor Au-Ag mineralization in these deposits. In combination with fluid inclusion homogenization temperatures, the results reveal the evolution of hydrothermal fluids and mechanisms of mineral precipitation. This study highlights the role of magmatic fluid inputs to formation of high-grade Au, Ag, and Te veins and the importance of correlating oxygen isotope analyses to fluid inclusion homogenization temperatures on the same generation of quartz in complex banded veins to reveal the source and evolution of ore-forming fluids.

2. Geologic setting

The Te-rich Sandaowanzi and Te-poor Dong'an epithermal Au-Ag deposits that are the focus of this study are located in the eastern part of the Paleozoic Central Asian Orogenic Belt (CAOB) (Sengör et al. 1993; Jahn et al. 2000; Jahn 2004; Li 2006). It consists of the Erguna and Xing'an Blocks in the northwest, the Songliao Block in the central part, and the Jiamusi Massif in the east, separated by the De'erbugan, Nenjiang-Hehei, and Jiayin-Mudanjiang structures, respectively (Fig. 1a; Wu et al. 2007). Sandaowanzi is in the Xing'an Block and Dong'an is in the Songliao Block (Fig. 1a).

The Xing'an Block is dominated by Early Cretaceous volcanic rocks (Ge et al. 2005; Sui et al. 2007; Zhang et al. 2010b; Gao et al. 2017, 2018a, b) and Neoproterozoic-Early Cambrian metamorphic rocks, e.g., Luomahu Group (Qu 2008; Fig. 1a). Although

DOI: https://doi.org/10.2138/am-2021-7825. http://www.minsocam.org/

sedimentation occurred during the Neoproterozoic and Paleozoic (Miao et al. 2004, 2007, 2015), metamorphism and deformation occurred in these blocks during the Jurassic (ca. 170-160 Ma; Miao et al. 2015). The Songliao Block is largely covered by Early Cretaceous volcanic rocks (Wang et al. 2002; Zhang et al. 2008) with local exposures of underlying granitoids and Proterozoic rocks (Wu et al. 2000, 2001; Wang et al. 2006; Pei et al. 2007; Gao et al. 2007; Zhang et al. 2008) (Fig. 1a).

Regional structures mainly consist of NE- and NW-trending faults. The Nenjiang-Heihe fault and Jiayin-Mudanjiang fault control the distribution of gold deposits in the area (Fig. 1a). Early Cretaceous intrusions consist of granite, granodiorite, and granite porphyry and have been dated at ca. 119-108 Ma (Gao et al. 2017, 2018b; Zhao et al., 2019). Although the ore ages are imprecise, Sandaowanzi, Dong'an and several other epithermal Au-Ag deposits in the area are interpreted to be coeval with a period of a ca. 122-108 Ma of Early Cretaceous volcanism (Ge et al. 2005; Sui et al. 2007; Zhang et al. 2010a; Gao et al. 2017, 2018a, b). Epithermal Au-Ag mineralization and contemporaneous volcanism occurred in an extensional setting related to subduction of the Paleo-Pacific Plate (e.g., Wu et al. 2005b).

2.1. Sandaowanzi

Sandaowanzi produced 22 t Au at an average grade of 14 g/t, 127 t Ag at an average

DOI: https://doi.org/10.2138/am-2021-7825. http://www.minsocam.org/

grade of 97 g/t, and 34 t of Te at an average grade of 17 g/t from gold-bearing quartz veins hosted in Early Cretaceous volcanic rocks (Yu et al. 2012; Xu et al. 2012; Liu et al. 2013; Zhai and Liu 2014; Gao et al. 2017). Sandaowanzi is hosted in the Lower Cretaceous Longjiang (121.7 Ma) Formation (Fm.). The lower and upper parts of the Longjiang Fm. contain pyroclastic and lava flow facies, respectively, with rock types comprising (brecciated) andesite and basaltic andesite. Geochemically, these igneous rocks are enriched in LREEs, Pb, K, and U, depleted in Nb, P, and Ti and are calc-alkaline (Gao et al. 2017). Major structures in the area include NW-SE- and E-W-trending faults, with most deposits localized along NW-trending normal faults. The E-W-trending faults are earlier than the volcanism and crosscut Jurassic intrusive rocks (Fig. 1b). The main igneous intrusion in the area is the gray, medium-grained, Sandaowanzi monzogranite (177.2 Ma; Gao et al. 2017). Near ore deposits, Sandaowanzi monzogranite was emplaced under Longjiang Fm. andesite (Fig. 1b). Diabase dikes (116.6 Ma; Liu et al. 2011) crosscut the ore bodies. The major ore type at Sandaowanzi consists of Au-Ag-telluride-bearing quartz veins. Ore bodies (40 in three ore belts) occur along WNW-trending normal faults in andesite flows and pyroclastic breccias of the Lower Cretaceous Longjiang Fm. (Fig. 1b). Ore body II is the only current operating stope. The lenticular ore body is 213 m long and 0.8-14.3 m thick (averaging ~6 m). It strikes 20-40°, dips 58-77°, and plunges 520 m deep along the dip direction. The average Au grade of ore body II is 13.98 g/t (Gao et al. 2017).

Five stages have been identified in the veins (Fig. 2a-e). Telluride minerals in the deposit include calaverite, krennerite, sylvanite, petzite, hessite, stützite, empressite, altaite and coloradoite, which coexist with chalcopyrite, sphalerite, tetrahedrite, galena, native gold, and minor pyrite and bornite. Other silver-bearing phases include acanthite, pyrargyrite, and kerargyrite. Petzite, sylvanite, calaverite, and native gold assemblages generally occur in bonanza ore veins, and silver-bearing minerals occur mostly in the upper parts of the ore bodies (Yu et al. 2012). Gold-Ag tellurides are the major gold-bearing minerals (>95% of Au production); the remaining ~5% is in native gold. Alteration minerals include quartz, pyrite, sericite, carbonates, anhydrite, chlorite, and epidote. Pyrite, albite, and chlorite are widespread in the alteration halo, which is ~15 m in width around the veins. Plagioclase is replaced by epidote, pyrite, calcite, sericite, and chlorite. Other alteration minerals include pyrophyllite and minor siderite. Veins contain quartz, calcite, and anhydrite with euhedral laumontite in vugs (Fig. 2f). Bulk oxygen isotope analyses indicate meteoric sources for the vein-forming fluids with $\delta^{18}O(Qz)$ ranging from -3.9 to -0.2, avg. -1.8 (Table 1; Wu et al. 2005a; Zhai et al. 2018). Sericite from the alteration halo yielded $^{40}Ar/^{39}Ar$ plateau, isochron, and total gas dates that overlap within error and yield a preferred age of 122.4 ± 3.9 Ma (Cheng 2017).

2.2. Dong'an

Dong'an produced 24 t Au at an average grade of 8.8 g/t and 207 t Ag at an average grade of 75.8 g/t from quartz-adularia veins hosted in Early Cretaceous volcanic rocks. Stratigraphy at Dong'an includes Lower Cretaceous Guanghua Fm. volcanic rocks and Oligocene-Pliocene sandstone and conglomerate. The Guanghua Fm. consists predominantly of rhyolitic lava and rhyolitic tuff with minor dacitic lava that are underlain by an Early Jurassic coarse- and fine-grained alkali feldspar granitic intrusion. The volcanic sequence and granitic intrusion are cut by granite porphyry dikes (Fig. 1c). The area is cut by a series of tensile-shear NS-, NE- and NNE-trending faults. The 14 gold orebodies recognized in the mine are controlled by NS- and NE-striking faults, dipping NW at 70 to 85°. Eight of the orebodies are hosted in rhyolitic lavas, five are hosted in rhyolitic porphyry dykes, and one is hosted in Jurassic granite. Gold-rich orebodies are commonly brecciated and the breccias are bounded by faults. The size of the gold veins varies considerably, from 50 to 800 m in length and 1 to 7 m in thickness. They extend to depths of less than 400 m and have grades from 3 to 10 g/t Au. The largest vein is 770 m long, 6.7 m thick on average, and has a vertical extent of 358 m, with an average grade of 8.8 g/t Au and 75.8 g/t Ag.

Ore minerals occur in sparse disseminations, local dense disseminations, isolated veinlets and stockworks inside the 1 to 7 m thick veins. Five stages have been identified in the veins (Fig. 3). Pyrite, galena, chalcopyrite, sphalerite, hematite, acanthite, native gold, electrum, and native silver are present in the ores (Fig. 4b). Altaite, petzite, hessite, and melonite are rare. Electrum (>95%) is the major gold- and silver-bearing mineral, with the remaining ~5% in Au-Ag tellurides. Quartz, adularia, chlorite, and calcite are the most abundant gangue minerals, with fluorite in places. The gold veins are enclosed by concentrically zoned alteration envelops consisting of quartz, chalcedonic quartz, sericite, adularia, chlorite, and pyrite. Bulk oxygen isotopes indicate meteoric sources for the vein-forming fluids with $\delta^{18}O(Qz)$ from -3.0 to 0.5, avg. -1.0 (Table 1; Ao et al. 2004; Yang 2008; Han 2013). Sericite yielded a $^{40}Ar/^{39}Ar$ date of 107.2 ± 0.6 Ma that is within uncertainty of a zircon U-Pb date of 108.1 ± 2.4 Ma on rhyolite porphyry (Zhang et al. 2010a).

3. Methods

3.1. Sampling and petrography

Samples used in this study were collected from vein exposures and drill holes in both vertical and horizontal directions at Sandaowanzi and Dong'an. The sample set includes barren and ore-bearing veins with different textures (Fig. 5; Table 2). Images of samples in reflected and transmitted light were obtained using petrographic microscope at the U.S. Geological Survey Denver Inclusion Analysis Laboratory. Thick sections (~200 µm) were used, because they are required for fluid inclusion studies. Although the birefringent colors of minerals in thick sections are different from standard thin sections under crossed polars, quartz textures are still evident. Representative samples were selected for

CL imaging.

3.2. SEM-CL and EDS

Cathodoluminescence (CL) images were acquired with a JEOL 5800LV scanning electron microscope (SEM) operated at 10 or 15 kV and approximately 5 nA beam current at the U.S. Geological Survey Denver Microbeam Laboratory. Double polished thick sections (~200 μm) and mineral mounts from 35 samples of banded vein material from Sandaowanzi and Dong'an were studied. The major element composition of adularia was determined by energy dispersive X-ray spectroscopy (EDS) with 50 mm^2 silicon drift detector on a FEI Quanta 450 FEG-SEM operated at 15 kV accelerating voltage. Beam calibration was performed on copper metal and Oxford factory standards. Orthoclase and albite standards were analyzed to check the calibration. The major element compositions of adularia were used to calculate secondary ion mass spectrometer (SIMS) bias corrections for $\delta^{18}O$ values.

3.3. Oxygen isotopes

The $\delta^{18}O$ values of quartz, chalcedony, and adularia from five representative samples were measured using a CAMECA IMS 1280 SIMS at the WiscSIMS Laboratory, University of Wisconsin-Madison (Kita et al. 2009; Valley and Kita 2009; Heck et al.

2011). Oxygen isotope ratios were analyzed using a 1.6 nA $^{133}Cs^{+}$ primary beam of ions focused to a spot of ~10 μm diameter. Analysis pits were 1-2 μm deep. Ions of $^{16}O^{-}$ and $^{18}O^{-}$ were simultaneously collected in two movable Faraday cup detectors with an average $^{16}O^{-}$ intensity of 2.7 × 10^{9} cps and $^{16}O^{1}H^{-}$ was collected in the axial Faraday cup to check for traces of water in quartz. The magnetic field strength was held stable using a nuclear magnetic resonance (NMR) probe, which was readjusted every 12 h. The mass resolving power (MRP = M/ΔM), measured at 10% peak height, for $\delta^{18}O$ analytical conditions was ~2200 for the movable Faraday detectors and ~5000 for the axial position, allowing $^{16}O^{1}H^{-}$ to be resolved from $^{17}O^{-}$ (Kita et al. 2009; Wang et al. 2014). Each spot analysis took approximately 4 min, which includes 10 s of presputtering to penetrate the gold coating, ~60 s to stabilize sputtering and automatically center the secondary ions in the field aperture, and 80 s (20 cycles of 4 s each) to integrate secondary ions. Detailed descriptions of these analytical conditions and the instrument setup at WiscSIMS have been published previously (Kelly et al. 2007; Kita et al. 2009; Valley and Kita 2009; Heck et al. 2011; Wang et al. 2014). All data were collected with a standard-sample-standard bracketing procedure of four UWQ-1 quartz-standard measurements, 10-16 sample measurements and four UWQ-1 standard measurements. Oster et al. (2017) showed that the SIMS bias is not measurably different for UWQ-1, an anhydrous quartz vs. the hydrous opal standard, BZVV. Bracketing standards were used to evaluate the reproducibility of a series of measurements as well as to correct for the instrumental bias and minor instrument drift. The external spot-to-spot reproducibility of

DOI: https://doi.org/10.2138/am-2021-7825. http://www.minsocam.org/

bracketing standards averaged ±0.22‰ (2 standard deviations, SD) for oxygen isotope analyses. Raw values of isotope ratios measured by SIMS were corrected to the Vienna standard mean oceanic water (VSMOW) scale for oxygen based on values measured for the UWQ-1 bracketing standards (UWQ-1: $\delta^{18}O$ = 12.33‰, VSMOW, Kelly et al. 2007; Heck et al. 2011). To ensure that the best precision and accuracy were achieved, all analyses were conducted on spots within 5 mm of the center of a polished 25 mm mount (Kita et al. 2009; Peres et al. 2013).

Four feldspar reference materials, Amelia Ab (Or% = 0), MES-4 (Or% = 71), FCS (Or% = 75), and Gem28 (Or% = 93), were measured in the same SIMS session to determine the bias as a function of major element chemistry (Pollington 2013). Because we use UWQ-1 as a bracketing standard, all calculations use the difference in the biases of quartz and feldspar to calculate VSMOW values of feldspar (adularia) (Pollington 2013). Relative bias to UWQ-1 of Amelia Ab was 3.87‰ for end member albite during the analysis session. The relative biases of FC, MES-4, and Gem28 were 4.76‰, 4.98‰, and 4.94‰ for K-feldspar, respectively (Appendix A). The mean measured UWQ-1 values are 5.94‰ for SG-1, 5.82‰ for SG-2, and 5.98‰ for SG-3, respectively. All measured feldspars (adularia) were measured with SG-3.

Values of $^{16}O^{1}H^{-}/^{16}O^{-}$ (OH/O hereafter) were background corrected for contaminant OH by subtracting the average OH/O values measured on bracketing analyses of UWQ-1 quartz standard that comes from a granulite facies quartzite and is assumed to be anhydrous (see Wang et al. 2014). Background corrected ratios of OH/O are not calibrated against a standard but are useful on a relative basis to identify subtle changes in OH content of silica (e.g., chalcedony) as well as aqueous solid and fluid inclusions.

3.4. Microthermometry

In each of the five representative samples, fluid inclusion assemblages observed in crystalline quartz were spatially correlated with the CL bands analyzed by SIMS. Fluid inclusion petrography and microthermometry were conducted at the U.S. Geological Survey Denver Inclusion Analysis Laboratory. A Linkman 600 heating/freezing stage on an Olympus BX60 microscope was used to measure the ice melting temperature and homogenization temperature of fluid inclusions in each assemblage. A pure H_2O standard with an ice melting temperature (T_m) of 0 °C and a critical homogenization temperature (T_h) of 373.6 °C was used to calibrate the stage with the data reproducible to ±0.2 °C for ice melting temperatures and ±2.0 °C for homogenization temperatures.

4. Results

4.1. Petrography of minerals

In this study, we describe quartz textures using terminology from Dong et al. (1995) for adularia-sericite epithermal deposits. Colloform (Fig. 6a-e), jigsaw (Fig. 6b), bladed (Fig. 7a), flamboyant (Fig. 7b), plumose (Fig. 7c), granoblastic and comb (Fig. 6c-e) textures were observed under crossed polars. Other textures such as zonal and cockade are evident on SEM-CL images.

At Sandaowanzi, colloform textures (Stage I) are barren of gold and consist of alternating bands of fine-grained quartz with a jigsaw texture and thin layers of quartz with a granoblastic texture (Fig. 6a, b). In thin section, jigsaw texture is characterized by aggregates of microcrystalline to coarse crystalline quartz crystals with interpenetrating grain boundaries (Fig. 6a, b). Fibrous chalcedony with sweeping extinction and a botryoidal texture (Stage II) also grows on, or is mantled by, quartz with a granoblastic texture (Fig. 6c). Intervening quartz layers with granoblastic and comb textures (Stage III; Fig. 6d, e) usually contain sparse liquid-rich fluid inclusions. Gold-silver telluride bands are associated with a thin overgrowth (Stage IV) on comb quartz (Fig. 6c-f).

At Dong'an, bladed texture (Stage I) consists of chalcedony and crystal quartz (Fig. 7a). Flamboyant texture (Stage II), followed by Stage III quartz and chalcedony, contains three dimensional arrays of small liquid- and vapor-rich inclusions that follow crystallographic axes (Fig. 7b). Plumose texture (Stage IV; Fig. 7c) consists of quartz and chalcedony overgrowths on euhedral adularia (Stage IV; Fig. 7d). Colloform textures

(Stage IV) are usually mineralized and consist of alternating bands of fine-grained quartz, coarse-grained quartz, chalcedony, and fine-grained adularia with electrum, pyrite, and sphalerite +/- trace amounts of Au-Ag tellurides (Fig. 7d, e, f).

4.2. Cathodoluminescence of minerals

Cathodoluminescence (CL) images were used to further document the paragenetic relationships among textures of, and zoning within quartz, chalcedony, adularia, and other gangue and ore minerals. The CL images shown in Figures 8 and 9 are of the thick sections that we used for SIMS $\delta^{18}O$ and fluid inclusion analyses. Textural complexity is clearly evident. In each panel, the white arrows show the direction of mineral growth with stages indicated by Roman numerals. Barren and high-grade material collected from the Sandaowanzi quartz-telluride veins is shown on Figure 8 and Dong'an quartz-adularia-electrum veins on Figure 9. Granoblastic and comb quartz is CL-gray (Fig. 8a-c), CL-dark, or CL-bright (Fig. 8d, e), whereas chalcedony is homogeneous and CL-dark (Fig. 8b, c). Adularia is also homogeneous and CL-dark relative to quartz (Fig. 9b, c). The multiple generations of quartz identified by CL at Sandaowanzi and Dong'an were grouped into five stages based on crosscutting relationships, growth zones, and mineral assemblages as described below.

At Sandaowanzi, the paragenetic sequence is (I) fine-grained quartz + coarse-grained

DOI: https://doi.org/10.2138/am-2021-7825. http://www.minsocam.org/

quartz, (II) chalcedony + CL-gray quartz + CL-dark quartz + CL-bright quartz, (III) CL-gray comb quartz + CL-dark zonal quartz, (IV) CL-bright quartz + CL-dark quartz + Au-Ag-tellurides, and (V) thin veinlets of CL-bright quartz (Fig. 8). Colloform textures are common at Sandaowanzi, and many are barren (Fig. 8a). Stage I has a colloform texture consisting of alternating fine-grained and coarse-grained quartz bands (Fig. 8a). Fine-grained quartz has a jigsaw texture in thin section, is CL-dark, and lacks fluid inclusions. Coarse-grained quartz is generally CL-gray and contains sparse tiny fluid inclusions. In high-grade veins, Stage I colloform quartz is sometimes brecciated and overgrown by Stage II chalcedony and crystalline quartz (e.g., Fig. 8b). In some sections, Stage II chalcedony forms circles that are overgrown by quartz (Fig. 8c). Stage III quartz consists of CL-gray comb and CL-dark zones that are overgrown by a Stage IV thin rim of CL-bright and dark quartz followed by Au-Ag-tellurides (Fig. 8c-e). Thin (20 ~ 120 μm in width), Stage V veinlets of CL-bright quartz are also present that crosscut the early stages (e.g., Fig. 8b). Fluid inclusions are present in Stages I, II, and III CL-gray and CL-bright quartz crystals.

At Dong'an, the paragenetic sequence is (I) bladed chalcedony + bladed quartz, (II) CL-dark quartz + CL-bright quartz, (III) chalcedony + CL-gray quartz + CL-bright quartz, (IV) adularia + chalcedony + CL-dark quartz + CL-gray quartz + electrum, and (V) thin veinlets of CL-dark and bright quartz (Fig. 9). Bladed quartz textures including ghost and lattice are common at Dong'an, and many are barren. Both chalcedony and bladed Stage I

DOI: https://doi.org/10.2138/am-2021-7825. http://www.minsocam.org/

quartz are CL-dark, whereas Stage II and III quartz are both CL-bright and CL-dark and can have a circular shape (Fig. 9a). Stage II quartz is sometimes brecciated and overgrown by Stage III of chalcedony, CL-gray, and CL-bright quartz with a cockade texture (e.g., Fig. 9b). In ore-bearing veins, earlier stages of quartz are typically brecciated and cemented with Stage IV adularia (Fig. 9b and c). Stage IV adularia is overgrown by chalcedony, CL-dark quartz and CL-gray comb quartz followed by electrum (Fig. 9c). Stage V veinlets of quartz are also present and crosscut the Stage II, III, and IV quartz bands (Fig. 9b and c). Stages I, II, and IV quartz contain fluid inclusions.

4.3. SIMS oxygen isotopes

SIMS oxygen isotope analyses of quartz, chalcedony and adularia from three samples at Sandaowanzi and two samples at Dong'an are presented in Appendix A and displayed on Figures 8-10. Sandaowanzi quartz and chalcedony have a wide range of $\delta^{18}O$ values from -7.1 to +7.7‰. A slight decrease from Stage I to Stage III is followed by an abrupt increase in Stage IV quartz, which is mantled by Au-Ag-tellurides (Fig. 10a). At Dong'an, quartz and chalcedony have a narrow range from -2.2 to +1.6‰, and adularia varies from -5.9 to -3.5‰ (Fig. 10b).

In Stage I barren colloform texture quartz at Sandaowanzi, $\delta^{18}O$ values fluctuate mildly along the direction of growth (Fig. 8a). Bands of fine-grained quartz (FQ, blue symbols) have $\delta^{18}O$ values that are 1-2‰ higher than those of more coarsely crystalline quartz (red symbols) (Fig. 8a). In contrast, the $\delta^{18}O$ values of Stage II CL-gray quartz and chalcedony are 3-4‰ lower than brecciated Stage I fine-grained quartz (Fig. 8b, c). Stage III CL-gray comb quartz also has $\delta^{18}O$ values that are 1-2‰ lower than Stage II CL-bright and CL-gray quartz and chalcedony (Fig. 8d, e). Notably, the Stage II quartz and chalcedony and Stage III CL-gray comb quartz have much lower $\delta^{18}O$ values (down to -7.1‰) than the rims of Stage IV CL-dark and CL-bright quartz followed by tellurides (e.g., Fig. 8d, e). The Stage V thin quartz veinlet has an $\delta^{18}O$ value of -2.4‰ (e.g., Fig. 8b).

In Stage I to Stage III barren ghost bladed textures at Dong'an, $\delta^{18}O$ values fluctuate from -2.2 to +1.6‰ with a median of -0.3‰ (Fig. 9a). In Stage II to Stage III silica bands with a cockade texture, $\delta^{18}O$ values have a narrow range from -2.1 to -0.2‰ (Fig. 9b). In ore-bearing veins, the $\delta^{18}O$ values of Stage IV quartz followed by electrum have a narrow range from -1.6 to -0.2‰ (Fig. 9c) that is within the range of values from the barren bands (Stage I to Stage III). Moreover, the Stage V thin quartz veinlet crosscutting silica bands and cockade texture also has $\delta^{18}O$ values from -1.1 to -0.1‰ that are similar to the other stages (Fig. 9b, c).

4.4. Fluid inclusion microthermometry

Fluid inclusion petrography and microthermometry were conducted on the same samples used for CL imaging and SIMS analysis, which enabled spatial correlation of homogenization temperatures with the $\delta^{18}O$ results obtained on specific bands of quartz. Fluid inclusions were only observed in crystalline quartz and they are uncommon (Fig. 11). None were observed in fine-grained quartz or chalcedony. Microthermometric measurements were generally made on inclusions more than 5 μm in diameter. Most of the inclusions were classified as primary; they have irregular shapes, occur along crystal growth zones, and are liquid-rich with 0 to 25 vol% vapor at room temperature. Secondary inclusions along fractures are also liquid-rich. Thus, the primary liquid-rich inclusions in crystal quartz were trapped prior to, or between, episodes of boiling. Microthermometric measurements on liquid-rich inclusions from each band are summarized in Table 3. All of the liquid-rich inclusions are dilute with salinities between 0 and 1.0 wt.% NaCl equiv. The homogenization temperatures (T_h) of primary liquid-rich inclusions vary from 237 to 281 °C (Fig. 12) and have higher temperatures than those of secondary inclusions with T_h from 164 to 216 °C. Entrapment temperature is approximately equal to homogenization temperature because of low pressure in epithermal systems (Hass, 1971). To evaluate this further, the pressure-corrected temperatures at the conditions of T_h = 250 °C and T_m = -0.5 °C are 251, 255, and 259 °C with the referred pressures of 50, 100, and 150 bars, respectively (Steele-MacInnis et al., 2012).

DOI: https://doi.org/10.2138/am-2021-7825. http://www.minsocam.org/

At Sandaowanzi, fluid inclusions in a band of Stage I quartz with barren colloform texture have a narrow range of high T_h from 268.6 to 270.2 °C (average 269.4 °C); three groups of secondary fluid inclusions with lower T_h are also present (Table 3). Stage II CL-bright quartz has a T_h range from 248.6 to 252.4 °C (avg. 250.9 °C). Fluid inclusions in two bands of Stage III CL-gray quartz have a narrow range of T_h with averages of 248.2 °C and 250.5 °C. The low $\delta^{18}O$ of fluids in equilibrium with such quartz suggest that it precipitated from exchanged meteoric water. In contrast, fluid inclusions in Stage III comb quartz followed by the Stage IV rim associated with Au-Ag-tellurides have higher average T_h values of 276.2, 266.4, and 277.5 °C (Table 3), and the $\delta^{18}O$ values of fluids in equilibrium with the Stage IV rim are much higher.

At Dong'an, fluid inclusions in Stage I quartz with a ghost bladed texture also have high T_h from 267.6 to 269.5 °C (avg. 268.6 °C) (Table 3). This temperature may be representative of fluids prior to boiling. Fluid inclusions in Stage II CL-bright quartz layers in colloform texture have T_h from 242.1 to 245.0 °C (avg. 243.4 °C). Similarly, the T_h of fluid inclusions in Stage IV CL-gray comb quartz followed by electrum vary between 237.2 and 255.7 °C (avg. 244.6 °C) and between 244.2 and 248.9 °C (avg. 246.6 °C) (Table 3), which are within the range of data from barren bands. These data indicate that the quartz and adularia bands associated with electrum precipitated at average temperatures, which is unlike Sandaowanzi.

5. Discussion

Box and whisker plots showing the $\delta^{18}O$ values of each stage of chalcedony, quartz, and adularia from Sandaowanzi and Dong'an are compared to one another on Figure 10 and discussed below. Both Sandaowanzi and Dong'an have similar initial $\delta^{18}O(Qz)$ values (~0‰, Stage-I; Fig. 10a, b) and fluid inclusion homogenization temperatures (~270 °C; Fig. 10c, d). These initial fluids ($\delta^{18}O(H_2O)$ = -8.6‰, Stage-I; Fig. 10e, f) are indicative of isotopically exchanged meteoric water (e.g., Hedenquist and Lowenstern 1994; Simmons 1995; John et al. 2003; Simmons et al. 2005) and are typical of most other adularia-sericite Au-Ag deposits in the world (e.g., Simmons 1995; Faure et al. 2002; John et al. 2003). The magmatic fluid signal is thought to be weak in these deposits, because the intrusive source is deep such that magmatic fluids are diluted by a much larger volume of meteoric water (e.g., Giggenbach 1992; Hedenquist and Lowenstern 1994; Simmons 1995; Simmons et al. 2005).

At Sandaowanzi, variations in the $\delta^{18}O$ of quartz from ~0‰ in Stage I, to ~-4‰ in Stage II, to ~-6‰ in Stage III, to ~+7‰ in Stage IV, to ~-3‰ in Stage V (Fig. 10a) show that, at the micron to millimeter scale only accessible by SIMS (10-μm spots), $\delta^{18}O$ fluctuates by 15‰. We infer that this fluctuation reflects a step change in the proportions of meteoric and magmatic and fluid in the veins (Fig. 10a). Evidence for the mixing of meteoric water with magmatic fluids is provided by the low $\delta^{18}O$ values of Stage II-III quartz, the high $\delta^{18}O$ value of Stage IV quartz followed by Au-Ag-tellurides, and the low $\delta^{18}O$ values of Stage V quartz veins (Fig. 10a). The abrupt positive $\delta^{18}O$ shift (up to +7.7) detected in Stage IV quartz followed by Au-Ag telluride minerals at Sandaowanzi (Figs. 8c-e and 10a) is similar to those attributed to input of magmatic fluids or vapors in other deposits (Giggenbach 1992; Hedenquist and Lowenstern 1994; Simmons 1995; Spry et al. 1996; Taylor 1997; Hedenquist et al. 1998; Simmons et al. 2005; Christie et al. 2007; Saunders et al. 2008; Simpson and Mauk 2011; Simmons et al. 2016).

Regarding ore-forming processes at Sandaowanzi, (i) colloform quartz veins (Stage I) are typical textures that form from boiling fluids and are thought to be a product of flashing-intense episodic boiling where the majority of the liquid transforms to steam (Moncada et al. 2012; Shimizu 2014; Simpson et al. 2015; Taksavasu et al. 2018). Layers of chalcedony and fine-grained quartz with a jigsaw texture are thought to form by recrystallization of an amorphous silica precursor that precipitated during episodes of boiling (Fournier 1985; Saunders 1990, 1994; Herrington and Wilkinson 1993; Saunders and Schoenly 1995; Shimizu et al. 1998; John et al. 2003; Shimizu 2014; Prokofiev et al. 2016). (ii) The small decrease in oxygen isotope ratios from Stage I to III indicates that hydrothermal fluids were still dominated by meteoric water (Fig. 10e). (iii) The subsequent increase by up to 15‰ during Stage IV records a substantial input of magmatic fluids into the veins. The euhedral comb textures of Stage III and IV quartz are

DOI: https://doi.org/10.2138/am-2021-7825. http://www.minsocam.org/

unlike typical textures that form from boiling fluids (e.g., bladed quartz, Dong et al. 1995; Moncada et al. 2012), which suggests that they precipitated from slowly changing conditions, such as fluid mixing or gentle boiling (a relatively small portion of the liquid mass is transferred to the vapor phase) or nonboiling (Fournier 1985; Dong et al. 1995; Moncada et al. 2012; Shimizu 2014; Taksavasu et al. 2018). Fluid inclusions in Stage III quartz (~280 °C) followed by the Stage IV rim have higher homogenization temperatures than those in Stage II quartz (~250 °C). (iv) After Stage IV magmatic fluid input, Stage V quartz $\delta^{18}O$ values decrease to -2.8‰, which reflects dilution by meteoric water with a calculated $\delta^{18}O(H_2O)$ = -12.3‰.

Although the positive oxygen isotope shift in Stage IV quartz could theoretically be explained by intense boiling with rapid cooling and oxygen isotope exchange with host rocks, textures (e.g., bladed quartz) with fluid inclusions (e.g., coexisting vapor-rich and liquid-rich) that form from boiling fluids are absent, and host rocks were sealed off by earlier stages of quartz. Fluid inclusion data also show that temperature increased (from 250 to 280 °C) in comb quartz followed by tellurides, which indicates that the positive oxygen isotope shift (15‰) was accompanied by heating rather than cooling. Furthermore, if the fluid moved through underlying metasedimentary rocks, they are unlikely to leach significant amounts of Te because of the low Te concentration in the crust (5 ppb; Wedepohl 1995). In addition, the subaerial continental setting of NE China in the Early Cretaceous precludes involvement of seawater in the hydrothermal systems.

Thus, the abrupt positive shift in $\delta^{18}O$ values in Stage IV quartz and the ensuing precipitation of Au-Ag telluride minerals must be due to a significant input of magmatic fluid.

To evaluate this further, the mixing ratios between hot (300, 325, and 350 °C) magmatic water and cooler 250 °C exchanged meteoric water required to produce a shift from Stage III (average -5‰) to Stage IV (max +7.7‰), are ~1.7/1, ~1.9/1, and ~2.2/1 at corresponding temperatures of 281, 299, and 318 °C, respectively (Fig. 13). These results show that mixing with 300 °C magmatic fluids is required to explain the $\delta^{18}O$(Qz) shift from -5 to 7.7‰ and the maximum temperature of ~278 °C recorded by fluid inclusions. Higher temperature magmatic fluids produce the same isotopic shift at much higher temperatures. Magmatic fluid must have been saturated with dissolved silica because it cooled from magmatic temperatures to 300 °C before mixing with 250 °C exchanged meteoric water. Because the difference in silica solubility between 300 °C magmatic fluid and 250 °C exchanged meteoric water is small, only a small amount of quartz precipitated followed by tellurides. The magmatic fluid must also have had a low salinity or the increase in temperature would have been accompanied by a marked increase in salinity, which is not observed. We therefore surmise that the magmatic fluid in this system consisted of low salinity condensed magmatic vapor with elevated Te, Au, and Ag contents, as postulated by Williams-Jones and Heinrich (2005).

At Dong'an, although five stages of quartz were also distinguished, the $\delta^{18}O$ values of quartz and chalcedony are much more consistent with a narrow range of -2.2 to +1.6‰ that is indicative of meteoric hydrothermal fluids (Fig. 10b). Although adularia has a lower range from -5.9 to -3.5‰ (Fig. 10b), this difference is mostly due to the ~3‰ fractionation factor between quartz and K-feldspar at epithermal conditions (Clayton et al. 1972, 1989; Chiba et al. 1989). In other words, adularia precipitated from the same fluid as quartz and chalcedony.

Regarding ore-forming processes at Dong'an, (i) Stage I bladed quartz is a pseudomorphic replacement of bladed calcite that formed by boiling of meteoric water (Simmons and Christenson 1994; Dong et al. 1995; Etoh et al. 2002a) and has oxygen isotope values that fluctuate over a range of ~2.0‰. (ii) Stage II flamboyant texture followed by Stage III quartz and chalcedony also forms from boiling fluids (Bodnar et al. 1985; Dong et al. 1995) and oxygen isotope compositions did not change much during precipitation of Stage II and III quartz and chalcedony. (iii) Subsequent boiling during Stage IV was accompanied by an increase in pH and precipitation of quartz, adularia, calcite, electrum, sphalerite, and galena with plumose and colloform textures (Reed 1982; Reed and Spycher 1985; Simmons and Browne 2000; Zhou et al. 2001; Etoh et al. 2002b; Shimizu 2014). Gold-Ag tellurides are notably rare or absent. Fluid inclusions in Stage IV quartz also have homogenization temperatures that are similar to those in Stage II quartz (~245 °C). (iv) Finally, although oxygen isotope evidence for inputs of magmatic fluid is not obvious, the trace amount of Au-Ag telluride minerals allows that inputs may have been minute inputs (Fig. 7f). These results confirm that boiling was the main mechanism of Au-Ag mineralization in Stage IV quartz-adularia-electrum bands at Dong'an, which is also similar to other adularia-sericite Au-Ag deposits in the world (e.g., Hishikari, Japan; Hayashi et al. 2001; Faure et al. 2002).

6. Implications

This study shows that detailed understanding of the textures, oxygen isotope compositions, homogenization temperatures, and salinities of fluid inclusions within paragenetically complex quartz veins can advance understanding of fluid sources and processes of mineral precipitation in Au-Ag ± Te bearing epithermal systems. The detailed CL patterns, oxygen isotope, and temperature variations documented in these quartz veins show that inputs of magmatic fluid into adularia-sericite epithermal systems are exceedingly difficult to detect without in situ micro analysis spatially correlated to textures. Furthermore, these minerals only record clear evidence of magmatic inputs in thin growth zones of quartz (20-100 μm) that are mantled by Au-Ag-Te minerals. Consequently, most of the evidence gathered from gangue minerals in these systems using conventional methods is apt to record convection and episodic boiling of more or less barren meteoric hydrothermal fluids. Our results support a growing body of evidence that productive high-grade Au-Ag-telluride ores in adularia-sericite epithermal systems form by the input of magmatic fluids into otherwise barren meteoric flow systems. This interpretation is consistent with that proposed to explain the origin of bonanza epithermal Au-Ag deposits in the Northern Great Basin, USA, based on the O and Pb isotope compositions of ore and gangue minerals (Saunders et al., 2008) and thus may have broad applicability.

Acknowledgements

The authors are grateful to the Bureau of Geology and Mineral Exploration (Heilongjiang), the Geological Brigades of the Heilongjiang Geological Survey, and Sandaowanzi and Dong'an Gold Co. Ltd. for their wholehearted support of the field work. Drs. Le Wang and Kaixuan Hui are thanked for their help on the sample collection. Drs. Richard J. Moscati, Thomas Monecke, Benjamin J. Linzmeier, and Mitchell Bennett are thanked for their help on the sample preparation, CL images, QGIS maps, and FIs homogenization temperatures. The manuscript benefited from reviews by James A. Saunders, an anonymous referee, and the U.S. Geological Survey reviewers Craig A. Johnson and Jeffrey L. Mauk. Daniel Gregory is thanked for careful editorial handling. This study was funded by the Natural Science Foundation of China (Grant No. 41802099), the National Key Research and Development Program of China (Grant No. 2017YFC0601306), the foundation of the Key Laboratory of Mineral Resources, IGGCAS (Grant No. KLMR2017-08), the CPSF-CAS Joint Foundation for Excellent

Postdoctoral Fellows (Grant No. 2017LH016), and the China Postdoctoral Science Foundation (Grant No. 2018M631567). WiscSIMS is supported by the U.S. National Science Foundation (EAR-1658823) and the University of Wisconsin- Madison. JWV and KK are supported by the U.S. Department of Energy, Office of Science, Office of Basic Energy Sciences (Geosciences) under Award Number DE-FG02-93ER14389. Any use of trade, product, or firm names is for descriptive purposes only and does not imply endorsement by the U.S. Government.

References cited list

Ahmad, M., Solomon, M., and Walshe, J. (1987) Mineralogical and geochemical studies of the Emperor gold telluride deposit, Fiji. Economic Geology, 82, 345–370.

Anderson, W.B., and Eaton, P.C. (1990) Gold mineralization at the Emperor Mine, Vatukoula, Fiji. Journal of Geochemical Exploration, 36, 267–296.

Ao, G., Xue, M., Zhou, J., Wang, G., and Chen, H. (2004) Genesis of Dong'an gold deposit, Heilongjiang province, NE China. Mineral Resources and Geology, 18, 118–121 (in Chinese with English abstract).

Beaty, D.W., Kelley, K.D., Silberman, M.L., and Thompson, T.B. (1996) Oxygen isotope geochemistry of a portion of the Cripple Creek hydrothermal system, Guidebook Series, Society of Economic Geologists, Inc., 26, 55–64.

Bodnar, R.J., Reynolds, T.J., and Kuehn, C.A., 1985, Fluid-inclusion systematics in epithermal systems, in Berger, B.R., and Bethke, P.M., eds., Geology and Geochemistry of Epithermal Systems, Society of Economic Geologists, Inc., p. 73–97.

Cernuschi, F., Dilles, J.H., Grocke, S.B., Valley, J.W., Kitajima, K., and Tepley, F.J., III (2018) Rapid formation of porphyry copper deposits evidenced by diffusion of oxygen and titanium in quartz. Geology, 46, 611–614.

Cheng, L. (2017) Ore genesis of the Sandaowanzi telluride-gold deposit in Heilongjiang province. M.Sc. thesis, Changchun, China, Jilin University, 36–38 (in Chinese with English abstract).

Chiba, H., Chacko, T., Clayton, R.N., and Goldsmith, J.R. (1989) Oxygen isotope fractionations involving diopside, forsterite, magnetite, and calcite: Application to geothermometry. Geochimica et Cosmochimica Acta, 53, 2985–2995.

Christie, A.B., Simpson, M.P., Brathwaite, R.L., Mauk, J.L., and Simmons, S.F. (2007) Epithermal Au-Ag and related deposits of the Hauraki goldfield, Coromandel volcanic zone, New Zealand. Economic Geology, 102, 785–816.

Ciobanu, C.L., Cook, N.J., and Spry, P.G. (2006) Preface – Special Issue: Telluride and selenide minerals in gold deposits – how and why?. Mineralogy and Petrology, 87, 163–169.

Clayton, R.N., Goldsmith, J.R., and Mayeda, T.K. (1989) Oxygen isotope fractionation in quartz, albite, anorthite, and calcite. Geochimica et Cosmochimica Acta, 53, 725–733.

Clayton, R.N., O'Neil, J.R., and Mayeda, T.K. (1972) Oxygen isotope exchange between quartz and water. Journal of Geophysical Research, 77, 3057–3067.

Cook, N.J., and Ciobanu, C.L. (2005) Tellurides in Au deposits: Implications for modelling, in Proceedings Mineral Deposit Research. Meeting the Global Challenge 2005, Springer, 1387–1390.

Cook, N.J., Ciobanu, C.L., Spry, P.G., and Voudouris, P. (2009) Understanding gold-(silver)-telluride-(selenide) mineral deposits. Episodes, 32, 249–263.

Cooke, D.R., and McPhail, D. (2001) Epithermal Au-Ag-Te mineralization, Acupan, Baguio district, Philippines: Numerical simulations of mineral deposition. Economic Geology, 96, 109–131.

Dong, G., Morrison, G., and Jaireth, S. (1995) Quartz textures in epithermal veins, Queensland; classification, origin and implication. Economic Geology, 90, 1841–1856.

Etoh, J., Izawa, E., and Taguchi, S. (2002b) A fluid inclusion study on columnar adularia from the Hishikari low-sulfidation epithermal gold deposit, Japan. Resource Geology, 52, 73–78.

Etoh, J., Izawa, E., Watanabe, K., Taguchi, S., and Sekine, R. (2002a) Bladed quartz and its relationship to gold mineralization in the Hishikari low-sulfidation epithermal gold deposit, Japan. Economic Geology, 97, 1841–1851.

Faure, K., Matsuhisa, Y., Metsugi, H., Mizota, C., and Hayashi, S. (2002) The Hishikari Au-Ag epithermal deposit, Japan: Oxygen and hydrogen isotope evidence in determining the source of paleohydrothermal fluids. Economic Geology, 97, 481–498.

Fekete, S., Weis, P., Driesner, T., Bouvier, A.S., Baumgartner, L., and Heinrich, C.A. (2016) Contrasting hydrological processes of meteoric water incursion during magmatic–hydrothermal ore deposition: An oxygen isotope study by ion microprobe. Earth and Planetary Science Letters, 451, 263–271.

Fournier, R.O. (1985) The behavior of silica in hydrothermal solution, in Berger, B.R., and Bethke, P.M., eds., Geology and Geochemistry of Epithermal Systems. Society of Economic Geologists, Inc., 45–61.

Friedman, I., and O'Neil, J.R. (1977) Compilation of stable isotope fractionation factors of geochemical interest, in Fleisher, M., ed., Data of Geochemistry (Sixth Edition): U.S. Geological Survey Professional Paper 440–KK, 11 p. https://doi.org/10.3133/pp440KK.

Gao, F.H., Xu, W.L., Yang, D.B., Pei, F.P., Liu, X.M., and Hu, Z.C. (2007) LA-ICP-MS zircon U-Pb dating from granitoids in southern basement of Songliao basin: Constraints on ages of the basin basement. Science in China (Series D), 50, 995–1004.

Gao, S. (2017) Study on Mesozoic gold metallogenic system, northern Heihe, Heilongjiang province. Ph.D. thesis, Beijing, China, China University of Geosciences (Beijing), 196 (in Chinese with English abstract).

Gao, S., Xu, H., Quan, S.L., Zang, Y.Q., Wang, T. (2018b) Geology, hydrothermal fluids, H-O-S-Pb isotopes, and Rb-Sr geochronology of the Daxintun orogenic gold deposit in Heilongjiang province, NE China. Ore Geology Reviews, 92, 569–587.

Gao, S., Xu, H., Zang, Y.Q., and Wang, T. (2018a) Mineralogy, ore-forming fluids and geochronology of the Shangmachang and Beidagou gold deposits, Heilongjiang province, NE China. Journal of Geochemical Exploration, 188, 137–155.

Gao, S., Xu, H., Zang, Y.Q., Yang, L.J., Yang, B., and Wang, T. (2017) Late Mesozoic magmatism and metallogeny in NE China: The Sandaowanzi-Beidagou example. International Geology Review, 59, 1413–1438.

Ge, W.C., Wu, F.Y., Zhou, C.Y., and Zhang, J.H. (2005) Zircon U-Pb ages and its significance of the Mesozoic granites in the Wulanhaote Region, central Great Xing'an Range. Acta Petrologica Sinica, 21, 749–762 (in Chinese with English abstract).

Giggenbach, W.F. (1992) Magma degassing and mineral deposition in hydrothermal systems along convergent plate boundaries. Economic Geology, 87, 1927–44.

Goldfarb, R.J., Berger, B.R., George, M.W., and Seal, R.R., II (2017) Tellurium, in Schulz, K.J., DeYoung, J.H., Jr., Seal, R.R., II, and Bradley, D.C., eds., Critical Mineral Resources of the United States—Economic and Environmental Geology and

Prospects for Future Supply. U.S. Geological Survey Professional Paper 1802, R1–R27.

Goldfarb, R.J., Hofstra, A.H., Simmons, S.F. (2016) Critical elements in Carlin, epithermal, and orogenic gold deposits, in Verplanck, P.L., and Hitzman, M.W., eds., Rare Earth and Critical Elements in Ore Deposits. Society of Economic Geologists, Inc., 217–244.

Haas, J.L. (1971) The effect of salinity on the maximum thermal gradient of a hydrothermal system at hydrostatic pressure. Economic Geology, 66, 940–946.

Han, S. (2013) Magmatic fluids and gold mineralization of the late Mesozoic epithermal gold system in northern Lesser Xing'an Range, NE China. Ph.D. dissertation, Changchun, China, Jilin University, 47–50 (in Chinese with English abstract).

Haroldson, E.L., Brown, P.E., Ishida, A., and Valley, J.W. (2020) SIMS oxygen isotopes indicate Phanerozoic fluids permeated a Precambrian gold deposit. Chemical Geology, 533, 119429.

Hayashi, K.I., Maruyama, T., and Satoh, H. (2001) Precipitation of gold in a low-sulfidation epithermal gold deposit: Insights from a submillimeter-scale oxygen isotope analysis of vein quartz. Economic Geology, 96, 211–216.

Heck, P.R., Huberty, J.M., Kita, N.T., Ushikubo, T., Kozdon, R., and Valley, J.W. (2011) SIMS analyses of silicon and oxygen isotope ratios for quartz from Archean and Paleoproterozoic banded iron formations. Geochimica et Cosmochimica Acta, 75, 5879–5891.

Hedenquist, J.W., and Lowenstern, J.B. (1994) The role of magmas in the formation of hydrothermal ore deposits. Nature, 370, 519–527.

Hedenquist, J.W., Arribas, A., Jr., and Reynolds, T.J. (1998) Evolution of an intrusion-centered hydrothermal system; Far southeast-Lepanto porphyry and epithermal Cu-Au deposits, Philippines. Economic Geology, 93, 373–404.

Herrington, R., and Wilkinson, J. (1993) Colloidal gold and silica in mesothermal vein systems. Geology, 21, 539–542.

Holwell, D.A., Fiorentini, M., McDonald, I., Lu, Y., Giuliani, A., Smith, D.J., Keith, M., and Locmelis, M. (2019) A metasomatized lithospheric mantle control on the metallogenic signature of post-subduction magmatism. Nature Communications, 10, 3511.

Jahn, B.M. (2004) The Central Asian Orogenic Belt and growth of the continental crust in the Phanerozoic, in Malpas, J., Fletcher, C.J.N., Ali, J.R., and Aitchison, J.C., eds., Aspects of the Tectonic Evolution of China. Geological Society, London, 73–100.

Jahn, B.M., Wu, F.Y., and Chen, B. (2000) Massive granitoids generation in central Asia: Nd isotopic evidence and implication for continental growth in the Phanerozoic. Episodes, 23, 82–92.

Jenkin, G.R.T., Graham, H., Smith, D.J., Khan, R., Abbott, A.P., Harris, R.C., Holwell, D.A., Graham, S.D., Khan, R., and Stanley, C.J. (2019) Gold and critical element recovery with environmentally benign Deep Eutectic Solvents. 15th SGA Biennial Meeting abstract, 4, 1512–1515.

Jensen, E.P., and Barton, M.D. (2000) Gold deposits related to alkaline magmatism, in Hagemann, S.G., and Brown, P.E., eds., Gold in 2000. Society of Economic Geologists, Inc., 279–314.

John, D.A., Hofstra, A.H., Fleck, R.J., Brummer, J.E., and Saderholm, E.C. (2003) Geologic setting and genesis of the Mule Canyon low-sulfidation epithermal gold-silver deposit, north-central Nevada. Economic Geology, 98, 425–463.

Keith, M., Smith, D.J., Doyle, K., Holwell, D.A., Jenkin, G.R.T., Barry, T.L., Becker, J., and Rampe, J. (2020) Pyrite chemistry: A new window into Au-Te ore-forming processes in alkaline epithermal districts, Cripple Creek, Colorado. Geochimica et Cosmochimica Acta, 274, 172–191.

Kelley, K.D., and Spry, P.G. (2016) Critical elements in alkaline igneous rock-related epithermal gold deposits, in Verplanck, P.L., and Hitzman, M.W., eds., Rare Earth and Critical Elements in Ore Deposits. Society of Economic Geologists, Inc., 195–216.

Kelley, K.D., Romberger, S.B., Beaty, D.W., Pontius, J.A., Snee, L.W., Stein, H.J., and Thompson, T.B. (1998) Geochemical and geochronological constraints on the genesis of Au-Te deposits at Cripple Creek, Colorado. Economic Geology, 93, 981–1012.

Kelly, J.L., Fu, B., Kita, N.T., and Valley, J.W. (2007) Optically continuous silcrete quartz cements of the St. Peter Sandstone: High precision oxygen isotope analysis by ion microprobe. Geochimica et Cosmochimica Acta, 71, 3812–3832.

Kita, N.T., Ushikubo, T., Fu, B., and Valley, J.W. (2009) High precision SIMS oxygen isotope analysis and the effect of sample topography. Chemical Geology, 264, 43–57.

Li, J.Y. (2006) Permian geodynamic setting of Northeast China and adjacent regions: Closure of the Paleo-Asian Ocean and subduction of the Paleo-Pacific Plate. Journal of Asian Earth Sciences, 26, 207–224.

Li, Z.Z., Qin, K.Z., Li, G.M., Jin, L.Y., Song, G.X., and Han, R. (2019) Incursion of meteoric water triggers molybdenite precipitation in porphyry Mo deposits: A case study of the Chalukou giant Mo deposit. Ore Geology Reviews, 109, 144–162.

Liu, J.L., Bai, X.D., Zhao, S.J., Tran, M.D., Zhang, Z.C., Zhao, Z.D., Zhao, H.B., and Lu, J. (2011) Geology of the Sandaowanzi telluride gold deposit of the northern Great Xing'an Range, NE China: Geochronology and tectonic controls. Journal of Asian Earth Sciences, 41, 107–118.

Liu, J.L., Zhao, S.J., Cook, N.J., Bai, X.D., Zhang, Z.C., Zhao, Z.D. and Lu, J. (2013) Bonanza-grade accumulations of gold tellurides in the Early Cretaceous Sandaowanzi deposit, northeast China. Ore Geology Reviews, 54, 110–126.

Miao, L.C., Fan, W.M., Zhang, F.Q., Liu, D.Y., Jian, P., Shi, G.H., Tao, H., and Shi, Y.R. (2004) Zircon SHRIMP geochronology of the Xinkailing-Kele complex in the northwestern Lesser Xing'an Range, and its geological implications. Chinese Science Bulletin, 49, 201–209.

Miao, L.C., Liu, D.Y., Zhang, F.Q., Fan, W.M., Shi, Y.R., and Xie, H.Q. (2007) Zircon SHRIMP U-Pb ages of the "Xinghuadukou Group" in Hanjiayuanzi and Xinlin areas and the "Zhalantun Group" in Inner Mongolia, Da Hinggan Mountains. Chinese Science Bulletin, 52, 1112–1124.

Miao, L.C., Zhang, F.Q., Zhu, M.S., and Liu, D.Y. (2015) Zircon SHRIMP U-Pb dating of metamorphic complexes in the conjunction of the Greater and Lesser Xing'an ranges, NE China: Timing of formation and metamorphism and tectonic implications. Journal of Asian Earth Sciences, 114, 634–648.

Moncada, D., Mutchler, S., Nieto, A., Reynolds, T.J., Rimstidt, J.D., and Bodnar, R.J. (2012) Mineral textures and fluid inclusion petrography of the epithermal Ag-Au deposits at Guanajuato, Mexico: Application to exploration. Journal of Geochemical Exploration, 114, 20–35.

O'Neil, J.R., and Silberman, M.L. (1974) Stable isotope relations in epithermal Au-Ag deposits. Economic Geology, 69, 902–909.

O'Neil, J.R., and Taylor, H.P., Jr. (1967) The oxygen isotope and cation exchange chemistry of feldspars. American Mineralogist, 52, 1414–1437.

Oster J. L., Kitajima K., Valley J. W., Rogers B. and Maher K. (2017) An evaluation of paired $\delta^{18}O$ and $(^{234}U/^{238}U)_0$ in opal as a tool for paleoclimate reconstruction in semi-arid environments. Chemical Geology, 449, 236–252.

Pei, F.P., Xu, W.L., Yang, D.B., Zhao, Q.G., Liu, X.M., and Hu, Z.C. (2007) Zircon U-Pb geochronology of basement metamorphic rocks in the Songliao Basin. Chinese Science Bulletin, 52, 942–948.

Peres, P., Kita, N.T., Valley, J.W., Fernandes, F., and Schuhmacher, M. (2013) New sample holder geometry for high precision isotope analyses: Surface and Interface Analysis, 45, 553–556.

Pollington A.D. (2013) Stable isotope signatures of diagenesis. natural and experimental studies. Ph.D. thesis, University of Wisconsin, Madison.

Prokofiev, V.Y., Kamenetsky, V.S., Selektor, S.L., Rodemann, T., Kovalenker, V.A., and Vatsadze, S.Z. (2016) First direct evidence for natural occurrence of colloidal silica in chalcedony-hosted vacuoles and implications for ore-forming processes. Geology, 45, 71–74.

Qu, G.S. (2008) Lithostratigraphy of Heilongjiang province, China. China University of Geosciences Press, Wuhan, China, 1–301 (in Chinese).

Reed, M.H. (1982) Calculation of multicomponent chemical equilibria and reaction processes in systems involving minerals gases and an aqueous phase. Geochimica et Cosmochimica Acta, 46, 513–528.

Reed, M.H. (1998) Calculation of simultaneous chemical equilibria in aqueous-mineral-gas systems and its application to modeling hydrothermal processes, in Richards, J.P., and Larson, P.B., eds., Techniques in Hydrothermal Ore Deposits Geology. Society of Economic Geologists, Inc., 10, 109–124.

Reed, M.H. and Spycher, N.F. (1985) Boiling, cooling, and oxidation in epithermal systems: A numerical modeling approach, in Berger, B.R., and Bethke, P.M., eds., Geology and Geochemistry of Epithermal Systems. Society of Economic Geologists, Inc., 249–272.

Saunders, J.A. (1990) Colloidal transport of gold and silica in epithermal precious-metal systems: Evidence from the Sleeper deposit, Nevada. Geology, 18, 757–760.

Saunders, J.A. (1994) Silica and gold textures in bonanza ores of the Sleeper deposit, Humboldt County, Nevada; evidence for colloids and implications for epithermal ore-forming processes. Economic Geology, 89, 628–638.

Saunders, J.A., and Brueseke, M.E. (2012) Volatility of Se and Te during subduction-related distillation and the geochemistry of epithermal ores of the western United States. Economic Geology, 107, 165–172.

Saunders, J.A., and Schoenly, P.A. (1995) Boiling, colloid nucleation and aggregation, and the genesis of bonanza Au–Ag ores of the Sleeper deposit, Nevada. Mineralium Deposita, 30, 199–210.

Saunders, J.A., Unger, D.L., Kamenov, G.D., Fayek, M., Hames, W.E., and Utterback, W.C. (2008) Genesis of middle Miocene Yellowstone hotspot-related bonanza epithermal Au–Ag deposits, Northern Great Basin, USA. Mineralium Deposita, 43, 715–734.

Sengör, A.M.C., Natal'in, B.A., and Burtman, V.S. (1993) Evolution of the Altaid tectonic collage and Paleozoic crustal growth in Eurasia. Nature, 364, 299–307.

Shelton, K.L., So, C.S., Haeussler, G.T., Chi, S.J., and Lee, K.Y. (1990) Geochemical studies of the Tongyoung gold-silver deposits, Republic of Korea; evidence of meteoric water dominance in a Te-bearing epithermal system. Economic Geology, 85, 1114–1132.

Shimizu, T. (2014) Reinterpretation of quartz textures in terms of hydrothermal fluid evolution at the Koryu Au-Ag deposit, Japan. Economic Geology, 109, 2051–2065.

Shimizu, T., Matsueda, H., Ishiyama, D., and Matsubaya, O. (1998) Genesis of epithermal Au-Ag mineralization of the Koryu mine, Hokkaido, Japan. Economic Geology, 93, 303–325.

Simmons, S.F. (1995) Magmatic contributions to low-sulfidation epithermal deposits, in Magmas, fluids and ore deposits. Mineralogical Association of Canada Short Course Series, 23, 455–477.

Simmons, S.F., and Browne, P.R.L. (2000) Hydrothermal minerals and precious metals in the Broadlands-Ohaaki geothermal system: Implications for understanding low-sulfidation epithermal deposits. Economic Geology, 95, 971–1000.

Simmons, S.F., and Christenson, B.W. (1994) Origins of calcite in a boiling geothermal system. American Journal of Science, 294, 361–400.

Simmons, S.F., Brown, K.L., and Tutolo, B.M. (2016) Hydrothermal transport of Ag, Au, Cu, Pb, Te, Zn, and other metals and metalloids in New Zealand geothermal systems: Spatial patterns, fluid-mineral equilibria, and implications for epithermal mineralization. Economic Geology, 111, 589–618.

Simmons, S.F., White, N.C., and John, D.A. (2005) Geological characteristics of epithermal precious and base metal deposits, in Hedenquist, J.W., Thompson, J.F.H., Goldfarb, R.J., and Richards, J.P., eds., One Hundredth Anniversary Volume, Society of Economic Geologists, Inc., 485–522.

Simpson, M.P., and Mauk, J.L. (2011) Hydrothermal alteration and veins at the epithermal Au-Ag deposits and prospects of the Waitekauri Area, Hauraki Goldfield, New Zealand. Economic Geology, 106, 945–973.

Simpson, M.P., Palinkas, S.S., Mauk, J.L., and Bodnar, R.J. (2015) Fluid inclusion chemistry of adularia-sericite epithermal Au-Ag deposits of the southern Hauraki Goldfield, New Zealand. Economic Geology, 110, 763–786.

Smith, M.P., Savary, V., Yardley, B.W.D., Valley, J.W. Royer, J.J., and Dubois, M. (1998) The evolution of the deep flow regime at Soultz-sous-Forfts, Rhine Graben, eastern France: Evidence from a composite quartz vein. Journal of Geophysical Research, 103, 27,223–27,237

Spry, P.G., Chryssoulis, S., and Ryan, C.G. (2004) Process mineralogy of gold: Gold from telluride-bearing ores. JOM, 56, 60–62.

Spry, P.G., Paredes, M.M., Foster, F., Truckle, J.S., and Chadwick, T.H. (1996) Evidence for a genetic link between gold-silver telluride and porphyry molybdenum mineralization at the Golden Sunlight deposit, Whitehall, Montana; fluid inclusion and stable isotope studies. Economic Geology, 91, 507–526.

Sui, Z.M., Ge, W.C., Wu, F.Y., Zhang, J.H., Xu, X.C., and Cheng, R.Y. (2007) Zircon U-Pb ages geochemistry and its petrogenesis of Jurassic granites in northeastern part of the Da Hinggan Mts. Acta Petrologica Sinica, 23, 461–480 (in Chinese with English abstract).

Steele-MacInnis, M., Lecumberri-Sanchez, P., and Bodnar, R.J. (2012) HOKIEFLINCS_H_2O-NACL: A Microsoft Excel spreadsheet for interpreting microthermometric data from fluid inclusions based on the PVTX properties of H_2O-NaCl. Computers & Geosciences, 49, 334–337.

Taksavasu, T., Monecke, T., and Reynolds, T. (2018) Textural characteristics of noncrystalline silica in sinters and quartz veins: Implications for the formation of bonanza veins in low-sulfidation epithermal deposits. Minerals, 8, 331.

Tanner, D., Henley, R.W., Mavrogenes, J.A., and Holden, P. (2013) Combining in situ isotopic trace element and textural analyses of quartz from four magmatic-hydrothermal ore deposits. Contributions to Mineralogy and Petrology, 166, 1119–1142.

Taylor, H.P. (1997) Oxygen and hydrogen isotope relationships in hydrothermal mineral deposits, in Barnes, H.L., ed., Geochemistry of Hydrothermal Ore Deposits. New York, Wiley–Interscience, 229–302.

Valley, J.W., and Graham, C.M. (1996) Ion microprobe analysis of oxygen isotope ratios in quartz from Skye granite: Healed micro-cracks, fluid flow, and hydrothermal exchange. Contributions to Mineralogy and Petrology, 124, 225–234.

Valley, J.W., and Kita, N.T. (2009) In situ oxygen isotope geochemistry by ion microprobe, in Fayek, M., ed., Secondary Ion Mass Spectrometry in the Earth Sciences: Gleaning the big picture from a small spot. Mineralogical Association of Canada, Short Course, 41, 19–63.

Valley, J.W., Graham, C.M., Harte, B., Kinny, P., and Eiler, J.M. (1998) Ion microprobe analysis of oxygen, carbon, and hydrogen isotope ratios, in McKibben, M.A., Shanks, W.C., III, and Ridley W.I., eds., Applications of Microanalytical Techniques to Understanding Mineralizing Processes: Society of Economic Geologists, Inc., 7, 73–98.

Voudouris, P. (2006) A comparative mineralogical study of Te-rich magmatic-hydrothermal systems in northeastern Greece. Mineralogy and Petrology, 87, 241–275.

Wang, P.J., Liu, Z.J., Wang, S.X., and Song, W.H. (2002) ^{40}Ar/^{39}Ar and K/Ar dating of the volcanic rocks in the Songliao basin, NE China: Constraints on stratigraphy and basin dynamics. International Journal of Earth Sciences, 91, 331–340.

Wang, X.L., Coble, M.A., Valley, J.W., Shu, X.J., Kitajima, K., Spicuzza, M.J., and Sun, T. (2014) Influence of radiation damage on Late Jurassic zircon from southern China: Evidence from in situ measurements of oxygen isotopes, laser Raman, U-Pb ages, and trace elements. Chemical Geology, 389, 122–136.

Wang, Y., Zhang, F.Q., Zhang, D.W., Miao, L.C., Li, T.S., Xie, H.Q., Meng, Q.R., and Liu, D.Y. (2006) Zircon SHRIMP U-Pb dating of meta-diorite from the basement of the Songliao Basin and its geological significance. Chinese Science Bulletin, 51, 1877–1883.

Wedepohl, K.H. (1995) The composition of the continental crust. Geochimica et Cosmochimica Acta, 59, 1217–1232.

Williams-Jones, A.E., and Heinrich, C.A. (2005) Vapor transport of metals and the formation of magmatic-hydrothermal ore deposits, in Hedenquist, J.W., Thompson, J.F.H., Goldfarb, R.J., and Richards, J.P., eds., One Hundredth Anniversary Volume, Society of Economic Geologists, Inc., 1287–1312.

Wu, F.Y., Lin, J.Q., Wilde, S.A., Zhang, X.O., and Yang, J.H. (2005b) Nature and significance of the Early Cretaceous giant igneous event in eastern China. Earth and Planetary Science Letters, 233, 103–119.

Wu, F.Y., Sun, D.Y., Li, H.M., and Wang, X.L. (2000) Zircon U-Pb ages of the basement rocks beneath the Songliao Basin, NE China. Chinese Science Bulletin, 45, 1514–1518.

Wu, F.Y., Sun, D.Y., Li, H.M., and Wang, X.L. (2001) The nature of basement beneath the Songliao Basin in NE China: Geochemical and isotopic constraints: Physics and Chemistry of the Earth. Part A. Solid Earth and Geodesy, 26, 793–803.

Wu, F.Y., Yang, J.H., Lo, C.H., Wilde, S.A., Sun, D.Y., and Jahn, B.M. (2007) The Heilongjiang Group: A Jurassic accretionary complex in the Jiamusi Massif at the western Pacific margin of northeastern China. Island Arc, 16, 156–172.

Wu, Z., Wang, H., Xu, D., and Zhou, Y. (2005a) Geology and geochemistry of the Sandaowanzi gold deposit, Heilongjiang province, NE China. Geological Review, 51, 264–267 (in Chinses with English abstract).

Xu, H., Yu, Y.X., Wu, X.K., Yang, L.J., Tian, Z., Gao, S., and Wang, Q.S. (2012) Intergrowth texture in Au-Ag-Te minerals from Sandaowanzi gold deposit Heilongjiang Province: Implications for ore-forming environment. Chinese Science Bulletin, 57, 2778–2786.

Yang, T. (2008) Volcanic rocks and their relationships to the gold mineralization in the Dong'an deposit, NE China. M.Sc. thesis, Beijing, China, China University of Geosciences (Beijing), 70–72 (in Chinese with English abstract).

Yu, Y.X., Xu, H., Wu, X.K., Yang, L.J., Tian, Z., Gao, S., and Wang, Q.S. (2012) Characteristics of the Au-Ag-Te minerals and its ore-forming fluids in Sandaowanzi gold deposit Heilongjiang Province. Acta Petrologica Sinica, 28, 345–356 (in Chinese with English abstract).

Zhai, D., and Liu, J. (2014) Gold-telluride-sulfide association in the Sandaowanzi epithermal Au-Ag-Te deposit, NE China: Implications for phase equilibrium and physicochemical conditions. Mineralogy and Petrology, 108, 853–871.

Zhai, D., Williams-Jones, A.E., Liu, J., Tombros, S.F., and Cook, N.J. (2018) Mineralogical fluid inclusion and multiple isotope (H-O-S-Pb) constraints on the genesis of the Sandaowanzi epithermal Au-Ag-Te deposit, NE China. Economic Geology, 113, 1359–1382.

Zhang, J.H., Gao, S., Ge, W.C., Wu, F.Y., Yang, J.H., Wilde, S.A., and Li, M. (2010b) Geochronology of the Mesozoic volcanic rocks in the Great Xing'an Range northeastern China: Implications for subduction–induced delamination. Chemical Geology, 276, 144–165.

Zhang, J.H., Ge, W.C., Wu, F.Y., Wilde, S.A., Yang, J.H., and Liu, X.M. (2008) Large-scale Early Cretaceous volcanic events in the northern Great Xing'an Range, northeastern China. Lithos, 102, 138–157.

Zhang, Z., Mao, J., Wang, Y., Pirajno, F., Liu, J., and Zhao, Z. (2010a) Geochemistry and geochronology of the volcanic rocks associated with the Dong'an adularia-sericite epithermal gold deposit, Lesser Hinggan Range, Heilongjiang province, NE China: Constraints on the metallogenesis. Ore Geology Reviews, 37, 158–174.

Zhao, Z.H., Sun, J.G., Li, G.H., Xu, W.X., Lü, C.L., Wu, S., Guo, Y., Liu, J., and Ren, L. (2019) Early Cretaceous gold mineralization in the Lesser Xing'an Range of NE China: The Yongxin example. International Geology Review, 61, 1522–1549.

Zhou, L., Guo, J., Liu, B., and Li, L. (2001) Structural state of adularia from Hishikari, Japan. Chinese Science Bulletin, 46, 950–953.

List of figure captions

Fig. 1. (a). Regional geologic map showing the location of Au-Ag deposits in north Heilongjiang province, NE China (after Gao 2017; Zhao et al. 2019). The inset shows the

location of the regional map relative to crustal blocks in NE China. Geologic map and cross section of Sandaowanzi (b) (after Liu et al. 2013; Gao et al. 2017) and Dong'an deposits (c) (after Zhang et al. 2010a).

Fig. 2. Photos of multiple generations of quartz from Sandaowanzi. (a). Stage I quartz veins hosted by andesite from underground. (b). Brecciated Stage I vein quartz cemented by the Stage II quartz from underground. (c). Stage II and Stage III quartz veins from underground. (d-e). Five stages of quartz and tellurides in the ore. (f). Early quartz vug with late euhedral laumontite. Roman numeral is quartz stage.
Abbreviations: Lmt=Laumontite. Qz=Quartz. SEE=Southeast-East.

Fig. 3. Photos of multiple generations of quartz from Dong'an. (a). Five generations of quartz with early bladed and late colloform textures in drill core. Early bladed textures cross-cut by late colloform textures. (b). Ore-bearing colloform textures from open pit. Stage I, II, II, IV quartz in vein hosted by altered rhyolite, and crosscut by Stage 5 thin quartz veinlets. (c). Stage IV quartz, chalcedony, and adularia crosscut by Stage V thin quartz veinlets from open pit. (d). Early bladed quartz textures that are barren of gold. (e). Colloform texture vein with four stages of quartz hosted in altered rhyolite. (f). Ore-bearing colloform vein. As in b, four stages of quartz are cut by Stage V thin quartz veinlets. Roman numeral is quartz stage.
Abbreviations: Adl=Adularia. Chc=Chalcedony. Lmt=Laumontite. Qz=Quartz.

Fig. 4. Paragenesis of ore and gangue minerals in the veins. (a). Sandaowanzi deposit. (b). Dong'an deposit.

Fig. 5. Sample locations from underground, open pit, and drill holes. (a). Longitudinal vertical projection of Sandaowanzi veins. (b). Plane map and cross section of Dong'an veins.

Fig. 6. Representative photomicrographs of quartz textures under crossed polars in transmitted light (a-e, sample thickness ~200 μm) and ore minerals in reflected light (f) from Sandaowanzi. (a). Colloform texture consisting of fine-grained quartz with a jigsaw texture and crystalline quartz with granoblastic texture. (b). Thin colloform texture with alternating bands of fine-grained jigsaw texture quartz and crystalline quartz. (c-e). Chalcedony, dark quartz, and crystalline quartz with a comb texture followed by tellurides. (f). Coarse-grained hessite, stützite, and petzite associated with comb quartz from figure d.

Abbreviations: Chc=Chalcedony. Qz=Quartz. Hes=Hessite. Ptz=Petzite. Stü=Stützite. CQ=Comb quartz. FQ=Fine-grained quartz.

Fig. 7. Representative photomicrographs of quartz textures under crossed polars in transmitted light (a-d, sample thickness ~200 μm) and ore minerals in reflected light (e-f)

from Dong'an. (a). Bladed quartz followed by chalcedonic quartz. (b). Quartz crystals with liquid- and vapor-rich inclusions in flamboyant texture. (c). Dark adularia crystals followed by plumose quartz. (d). Adularia and quartz bands with sulfides, tellurides, and electrum. (e). Pyrite, sphalerite, argentite, and electrum in colloform bands from figure d. (f). Rare fine-grained hessite, petzite, altaite, and electrum.

Abbreviations: Act=Acanthite. Adl=Adularia. Alt=Altaite. Chc=Chalcedony. Elc=Electrum. Gn=Galena. Hes=Hessite. Ptz=Petzite. Py=Pyrite. Qz=Quartz. Sp=Sphalerite. BQ=Bladed quartz. PQ=Plumose quartz.

Fig. 8. CL images of quartz and chalcedony from Sandaowanzi. SIMS oxygen isotope spots are in red, and homogenization temperatures of fluid inclusion assemblages are outlined in yellow. The orange dashed lines show how each band of quartz correlates with the oxygen isotope profile in red and corresponding fluid composition in blue. The quartz-water fractionation factor from Clayton et al. (1972) and Friedman and O'Neil (1977) and fluid inclusion homogenization temperature from each band were used to calculate $\delta^{18}O(H_2O)$. In bands where fluid inclusions are absent, temperature data from adjacent bands were used. (a). Colloform quartz with thin layer. (b and c). Fine-grained, drusy, and chalcedonic quartz without tellurides (b) and with abundant tellurides (c). (d and e). Chalcedonic, fine-grained, and crystal quartz with abundant tellurides.

Abbreviations: Chc=Chalcedony. Qz=Quartz. FQ=Fine-grained quartz. QB=Quartz with CL-bright. QD=Quartz with CL-dark. QG=Quartz with CL-gray. QV=Quartz vein (Thin).

DOI: https://doi.org/10.2138/am-2021-7825. http://www.minsocam.org/

Fig. 9. CL images of quartz, chalcedony and adularia at Dong'an. SIMS oxygen isotope spots are in red, and homogenization temperatures of fluid inclusion assemblages are outlined in yellow. The orange dashed lines show how each band of quartz correlates with the oxygen isotope profile in red and corresponding fluid composition in blue. The quartz-water fractionation factor from Clayton et al. (1972) and Friedman and O'Neil (1977) and fluid inclusion homogenization temperature from each band were used to calculate $\delta^{18}O(H_2O)$. The K-feldspar-water fractionation factor from O'Neil and Taylor (1967) fluid inclusion homogenization temperature from quartz in the same band with adularia were used to calculate $\delta^{18}O(H_2O)$. In bands where fluid inclusions are absent, temperature data from adjacent bands were used. (a). Barren ghost-bladed texture quartz. (b and c). Colloform and cockade texture (b) and colloform texture (c) with minor Au-Ag minerals.

Abbreviations: Adl=Adularia. Chc=Chalcedony. Qz=Quartz. QB=Quartz with CL-bright. QD=Quartz with CL-dark. QG=Quartz with CL-gray. QV=Quartz vein (Thin).

Fig. 10. Box and whisker plots of SIMS $\delta^{18}O$ data from chalcedony, quartz, and adularia in the Sandaowanzi and Dong'an deposits. (a and b). Measured $\delta^{18}O$ data. (c and d). Homogenization temperature of fluid inclusions spatially correlated to measured $\delta^{18}O$ data from each band. (e and f). Calculated $\delta^{18}O(H_2O)$ for every SIMS spot. (a, c, and e). Sandaowanzi. (b, d, and f). Dong'an. The orange dashed lines separate each stage.

Abbreviations: FQ=Fine-grained quartz. Adl=Adularia. Chc=Chalcedony. Qz=Quartz. QB=Quartz with CL-bright. QD=Quartz with CL-dark. QG=Quartz with CL-gray. QV=Quartz vein (Thin).

Fig. 11. Images of fluid inclusion assemblages with their average (Avg.) homogenization temperatures (T_h) from Sandaowanzi (a-c) and Dong’an (d-f). (a). Fluid inclusion assemblages from thin colloform texture shown on Figure 8a. (b). Fluid inclusion assemblages from CL-bright quartz shown on Figure 8d. (c). Fluid inclusion assemblages from CL-dark quartz near tellurides shown on Figure 8d, e. (d). Fluid inclusion assemblages from ghost-bladed texture shown on Figure 9a. (e). Fluid inclusion assemblages form CL-bright quartz breccia shown on Figure 9b. (f). Fluid inclusion assemblages form CL-gray quartz near electrum shown on Figure 9c.

Fig. 12. Histograms of fluid inclusion homogenization temperatures from Sandaowanzi and Dong’an deposits. Red color is primary fluid inclusions, blue color is secondary fluid inclusions.

Fig. 13. Diagrams showing the calculated fluid temperature and oxygen isotopic composition of water and quartz as a function of the mixing ratio of magmatic and meteoric water. Meteoric water has an initial temperature of 250 °C (based on stage III quartz fluid inclusion measurements at Sandaowanzi), and magmatic water has an initial

temperature of 300 (a), 325 (b), and 350 °C (c), respectively. Oxygen isotope values are 8‰ for magmatic water (Taylor 1997), and -14.7‰ for meteoric water (after stage III quartz at Sandaowanzi). The temperature of the mixed fluids is based on the enthalpy of water and the mixing increment. The effects of salinity on the enthalpy of water can generally be ignored because they are small (Reed 1998). Because the total mass of precipitated minerals is small in most cases, their heat contributions can be neglected (Reed 1998). The quartz-water fractionation factor used is from Clayton et al. (1972) as corrected by Friedman and O'Neil (1977).

List of tables

Table 1. Bulk oxygen isotope compositions from Sandaowanzi and Dong'an deposits.

Table 2. Compilation of the sample material, mineralogy, and applied analytical techniques.

Table 3. Microthermometric data on fluid inclusions from Sandaowanzi and Dong'an deposits.

Appendix A

Table A1. SIMS oxygen isotope data on quartz, chalcedony, and adularia from Sandaowanzi and Dong'an deposits.

Table 1. Bulk oxygen isotope compositions from Sandaowanzi and Dong'an deposits.

Location	Mineral	$\delta^{18}O_{SMOW}$	$\delta^{18}O_{H2O}$	Referred T (°C)	Reference
Sandaowanzi	Quartz in vein	-2.3	-14.7	190	Wu et al., 2005
	Quartz in vein	-2	-13.3	207	
	Quartz in vein	-1.8	-11.4	237	
	Quartz in vein	-0.2	-11.3	210	
	Quartz in vein	-1.8	-11.4	238	
	Quartz in vein	-2.2	-11.6	240	
	Quartz in vein	-0.7	-10.9	226	
	Quartz in vein	-1.5	-9.3	276	
	Quartz in vein	-1.7	-10.6	252	
	Quartz in vein	-1.9	-11	247	
	Quartz in vein	-2.5	-10.6	326	Zhai et al., 2018
	Quartz in vein	-0.4	-8.3	276	
	Quartz in vein	-0.3	-10.1	276	
	Quartz in vein	-1.9	-9.7	275	
	Quartz in vein	-3.3	-12.9	242	
	Quartz in vein	-1.8	-9.8	246	
	Quartz in vein	-3.9	-12	246	
	Quartz in vein	-0.3	-7.6	246	
	Quartz in vein	-3.5	-13.6	203	
	Quartz in vein	-2.6	-10.9	195	
Dong'an	Quartz in igneous rock	6.9	5.3	550	Han, 2013
	Quartz in igneous rock	7.5	5.9	550	
	Quartz in vein	0	-8.9	250	
	Quartz in vein	0.1	-8.9	250	
	Quartz in vein	-1.8	-10.9	250	
	Quartz in vein	-1.1	-12.8	180	
	Quartz in vein	0.3	-10.1	250	Ao et al., 2004
	Quartz in vein	-1.1	-8.5	250	
	Quartz in vein	0.5	-10.3	250	
	Quartz in vein	-1.3	-11.1	250	
	Quartz in vein	-2.1	-10.5	250	
	Quartz in vein	-1.5	-11.1	250	
	Quartz in vein	-3	-10.7	280	Yang, 2008
	Quartz in vein	-2.1	-10.6	250	
	Quartz in vein	-1.6	-10.5	250	
	Quartz in vein	-1.5	-9.6	250	
	Quartz in vein	-0.6	-7.5	250	
	Quartz in vein	1.5	-10.1	250	

This is the peer-reviewed, final accepted version for American Mineralogist, published by the Mineralogical Society of America.
The published version is subject to change. Cite as Authors (Year) Title. American Mineralogist, in press.
DOI: https://doi.org/10.2138/am-2021-7825. http://www.minsocam.org/

Table 2. Compilation of the sample material, mineralogy, and applied analytical techniques.

Site	Sample no.	Type	Ore texture	Mineralogy	Hot-CL	SEM-CL	SIMS	FIs
Sandaowanzi	130-1	High-grade	Comb	Quartz and tellurides		√		
	130CM21-6	Barren	Comb	Quartz		√		
	130CM23-10	Barren	Colloform	Quartz	√	√	√	√
	130CM23-14-1	High-grade	Multistage including colloform, coarse-grained, and comb	Quartz, chalcedony, and tellurides	√	√		
	130CM23-14-2	High-grade	Multistage including colloform, coarse-grained, and comb	Quartz, chalcedony, and tellurides	√	√	√	√
	130CM23-14-7	High-grade	Multistage including colloform, coarse-grained, and comb	Quartz, chalcedony, and tellurides	√	√	√	√
	130CM23-21	Barren	Colloform	Quartz	√	√		
	130CM23-4	Barren	Coarse-grained	Quartz		√		
	130CM23-5	Barren	Colloform	Quartz		√		
	170CM3	Barren	Comb	Quartz		√		
	210CM11-7	Barren	Coarse-grained	Quartz		√		
	210CM4	Barren	Comb quartz vein cross cutting andesite	Quartz		√		
	240CM10-3	Barren	Coarse-grained	Quartz	√	√		
	240CM9	Barren	Comb quartz vein cross cutting andesite	Quartz		√		
	50CM31	Barren	Coarse-grained	Quartz		√		
	50CM35-5	Barren	Coarse-grained	Quartz		√		
	90CM11	Barren	Coarse-grained	Quartz		√		
	90CM21-1	High-grade	Comb	Quartz and tellurides	√	√		
	90CM4	Barren	Coarse-grained	Quartz		√		
	SDW25B	High-grade	Multistage including colloform, coarse-grained, and comb	Quartz, chalcedony, and tellurides		√		
Dong'an	17-2-187	Barren	Coarse-grained	Quartz	√			
	18-1-164	Low-grade	Colloform	Quartz, chalcedony, adularia, and electrum	√	√		
	DA-100	Barren	Bladed and flamboyant	Quartz	√			
	DA-103	Barren	Coarse-grained	Quartz	√	√		
	DA-106	Barren	Coarse-grained	Quartz	√			
	DA-107	Barren	Colloform	Quartz, chalcedony, and adularia	√			
	DA-135	Low-grade	Colloform	Quartz, chalcedony, adularia, and electrum	√			
	DA-144	Barren	Comb	Quartz	√			
	DA-35	Barren	Coarse-grained	Quartz	√			
	DA-47	Barren	Colloform	Quartz and chalcedony	√			
	DA-53	Barren	Bladed and flamboyant	Quartz, chalcedony, and adularia	√	√	√	√
	DA-66	Barren	Colloform	Quartz and chalcedony	√			
	DA-77	Low-grade	Colloform	Quartz, chalcedony, adularia, and electrum		√		
	DA-80	Low-medium-grade	Colloform	Quartz, chalcedony, adularia, and electrum	√	√	√	√
	DA-90	Low-grade	Colloform	Quartz, chalcedony, adularia, and electrum	√			

Table 3. Microthermometric data on fluid inclusions from Sandaowanzi and Dong'an deposits.

Location	Sample no.	Area no.	Host mineral	CL	Stage	Assemblage no.	Type	Homogenization (T_h)	Ice melting ($T_{m, ice}$)
Sandaowanzi	130CM23-14-7	A_3	Quartz	Bright	II	G_1	L-V	256.1	-0.1
							L-V	255.2	-0.1
							L-V	256.6	-0.1
							L-V	255.8	-0.1
							L-V	257.1	-0.1
						G_2	L-V	257.2	-0.1
							L-V	257.9	-0.1
		A_5	Quartz	Dark	III	G_1	L-V	267.1	-0.3
							L-V	265.7	-0.3
							L-V	266.3	-0.3
		A_4	Quartz	Dark	III	G_1	L-V	272.8	-0.4
							L-V	278.8	-0.4
							L-V	280.8	-0.4
		A_1	Quartz	Gray	II	G_2	L-V	248.6	-0.3
							L-V	252.4	-0.3
						G_3	L-V	203.2	-0.5
							L-V	200.4	-0.1
		A_2	Quartz	Gray	II	G_1	L-V	248.5	-0.2
							L-V	254.7	-0.2
							L-V	249.6	-0.2
	130CM23-14-2	A_1	Quartz	Gray	II	G_1	L-V	244.8	-0.4
							L-V	251.6	-0.4
		A_2	Quartz	Dark	III	G_2	L-V	273.4	-0.4
							L-V	277.9	-0.4
							L-V	277.4	-0.4
	130CM23-21	A_1	Quartz	Gray	Secondary	G_1	L-V	167.3	-0.1
							L-V	168.4	-0.1
		A_2	Quartz	Gray	Secondary	G_1	L-V	216.4	-0.3
							L-V	213.6	-0.3
		A_3	Quartz	Gray	Secondary	G_1	L-V	187.5	-0.4
							L-V	185.2	-0.4
		A_4	Quartz	Gray	I	G_1	L-V	268.6	-0.3
							L-V	269.5	-0.3
							L-V	270.2	-0.3
Dong'an	DA-80	A_1	Quartz	Gray	IV	G_1	L-V	237.2	-0.3
							L-V	255.7	-0.3
							L-V	240.8	-0.3
						G_2	L-V	248.9	-0.3
							L-V	244.2	-0.3
		A_2	Quartz	Bright	II	G_1	L-V	242.1	-0.1
							L-V	245	-0.1
							L-V	243.2	-0.1
	DA-53	A_1	Quartz	Bright	Secondary	G_1	L-V	166.1	-0.6
							L-V	172.9	-0.6
							L-V	175.8	-0.6
							L-V	164.3	-0.6
					I	G_2	L-V	269.5	-0.1
							L-V	267.6	-0.1
		A_2	Quartz	Bright	Secondary	G_1	L-V	202.1	-0.3
							L-V	210.4	-0.3
							L-V	207.5	-0.3

This is the peer-reviewed, final accepted version for American Mineralogist, published by the Mineralogical Society of America.
The published version is subject to change. Cite as Authors (Year) Title. American Mineralogist, in press.
DOI: https://doi.org/10.2138/am-2021-7825. http://www.minsocam.org/

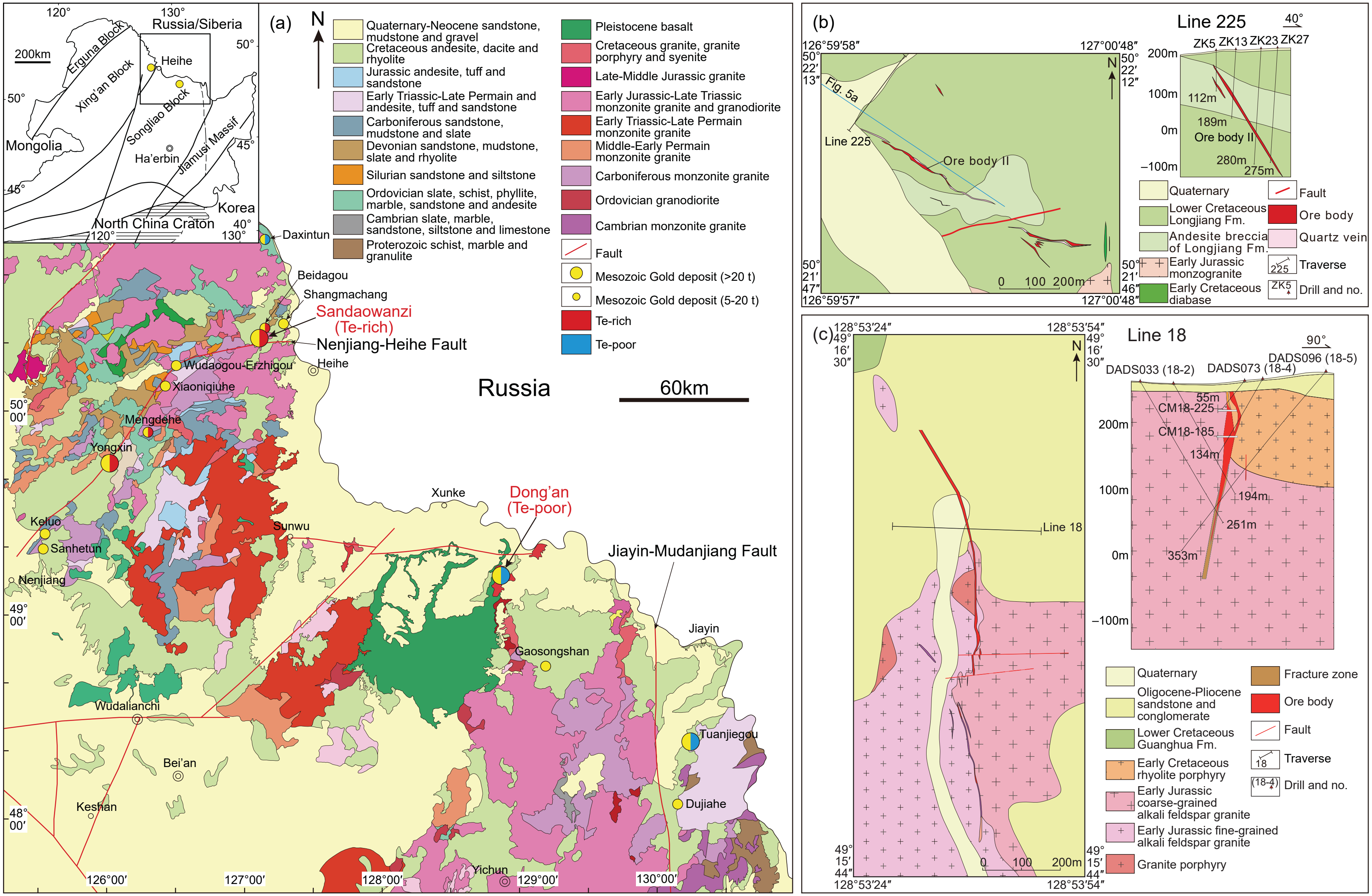

Fig. 1

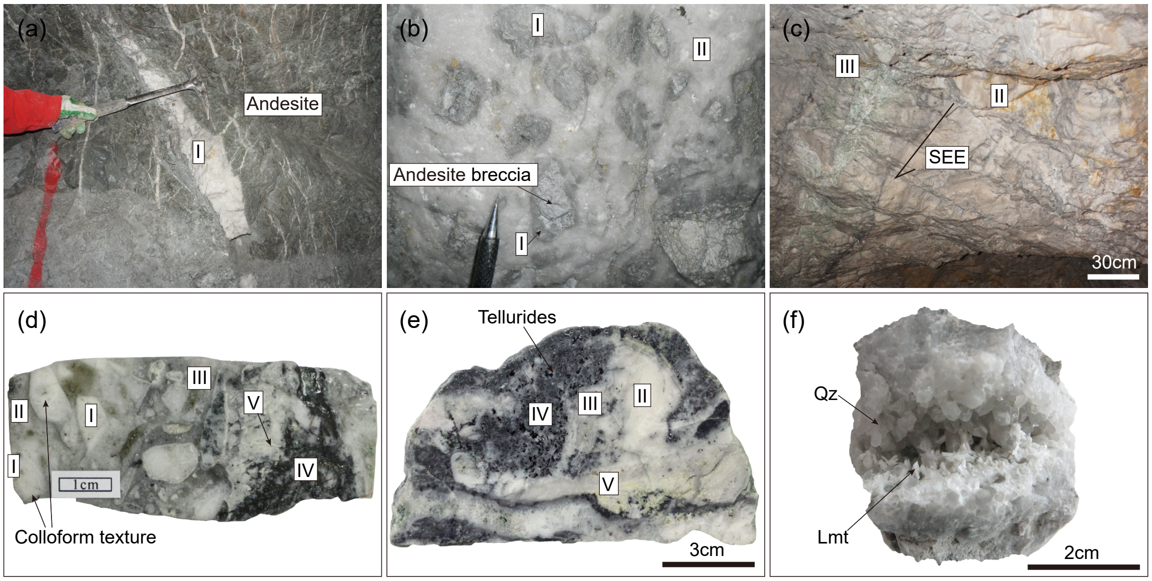
(a)
Andesite
I
(b)
I
II
Andesite breccia
I
(c)
III
II
SEE
30cm
(d)
III
II
I
V
I
IV
1cm
Colloform texture
(e)
Tellurides
IV
III
II
V
3cm
(f)
Qz
Lmt
2cm

Fig. 2

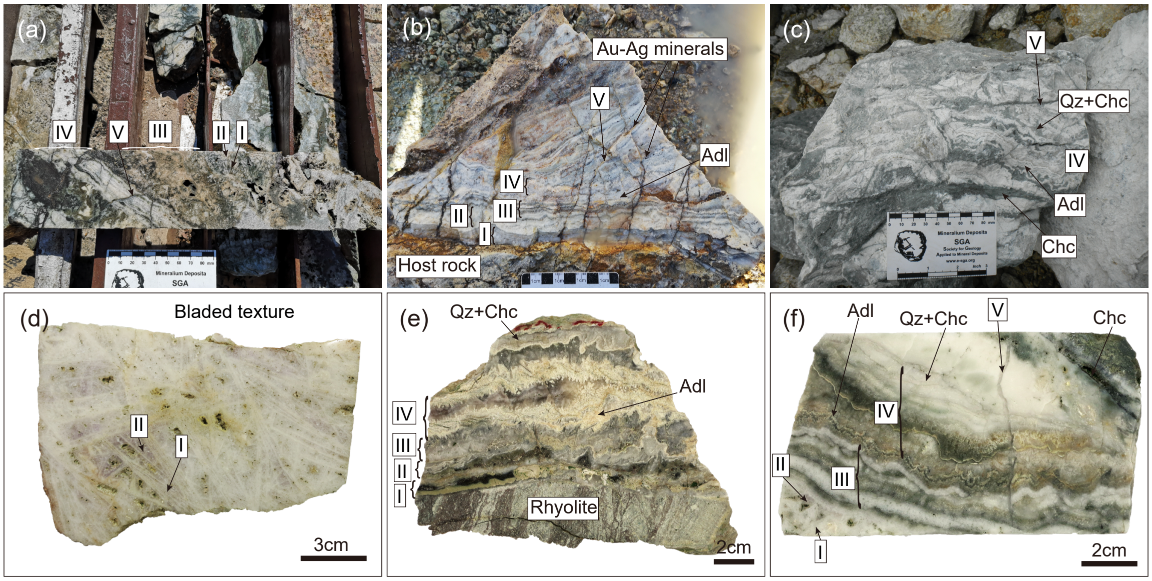
(a)
IV
V
III
II
I
(b)
Au-Ag minerals
V
Adl
IV
III
II
I
Host rock
(c)
V
Qz+Chc
IV
Adl
Chc
(d)
Bladed texture
II
I
3cm
(e)
Qz+Chc
Adl
IV
III
II
I
Rhyolite
2cm
(f)
Adl
Qz+Chc
V
Chc
IV
II
III
I
2cm

Fig. 3

DOI: https://doi.org/10.2138/am-2021-7825. http://www.minsocam.org/

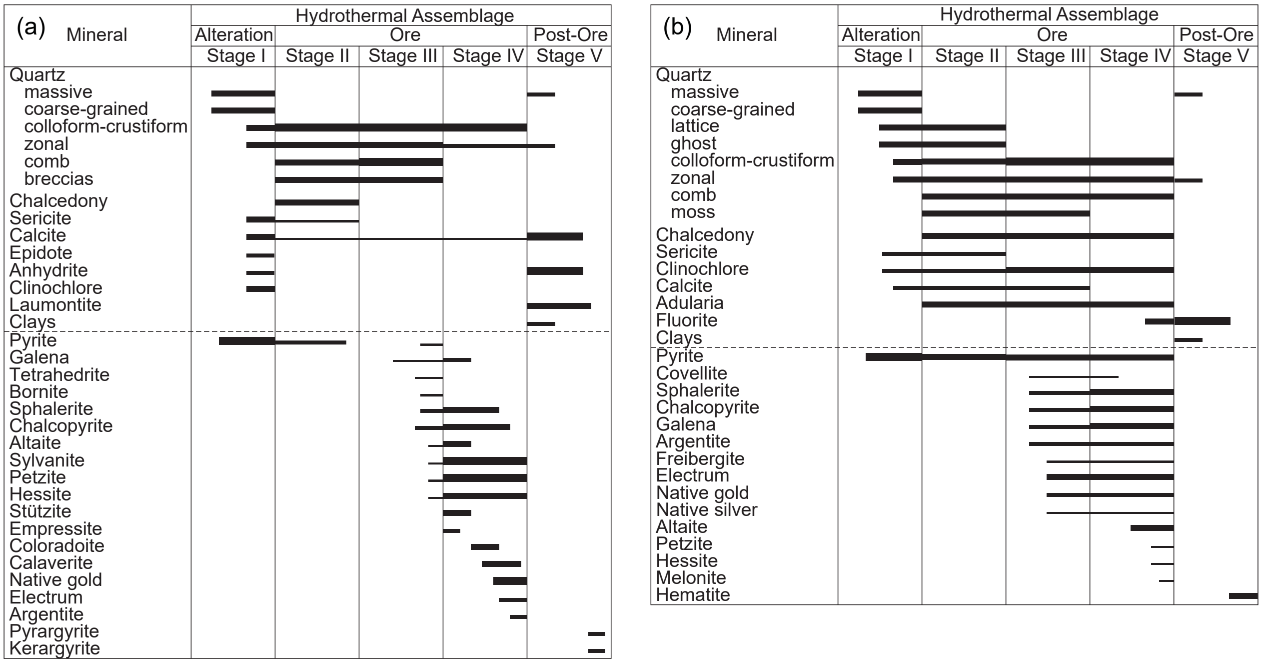

Fig. 4

This is the peer-reviewed, final accepted version for American Mineralogist, published by the Mineralogical Society of America.
The published version is subject to change. Cite as Authors (Year) Title. American Mineralogist, in press.
DOI: https://doi.org/10.2138/am-2021-7825. http://www.minsocam.org/

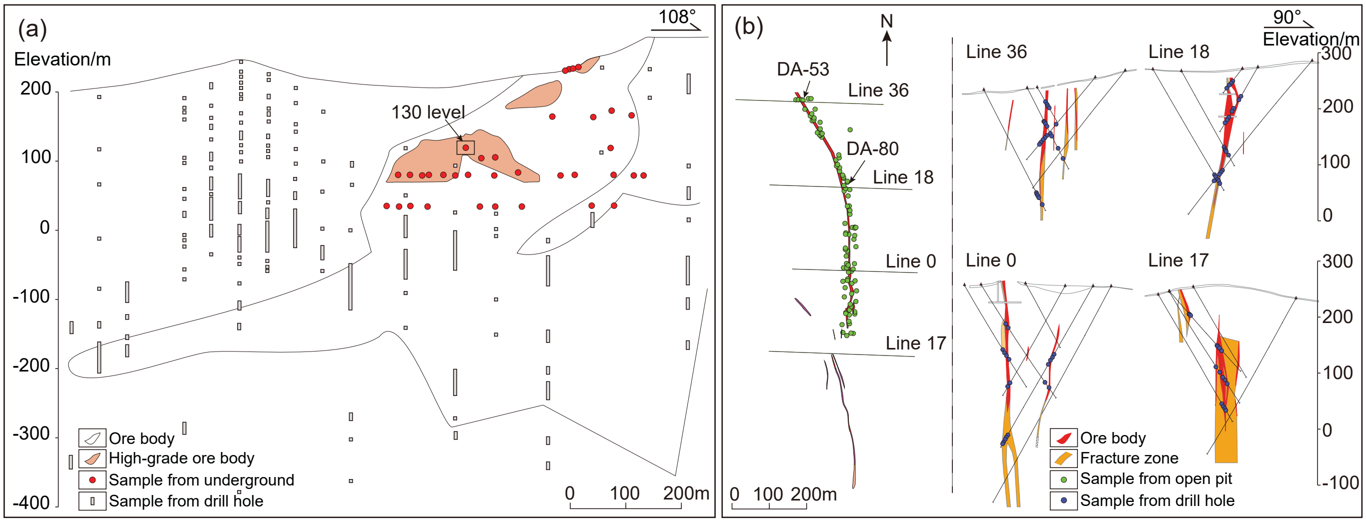

Fig. 5

DOI: https://doi.org/10.2138/am-2021-7825. http://www.minsocam.org/

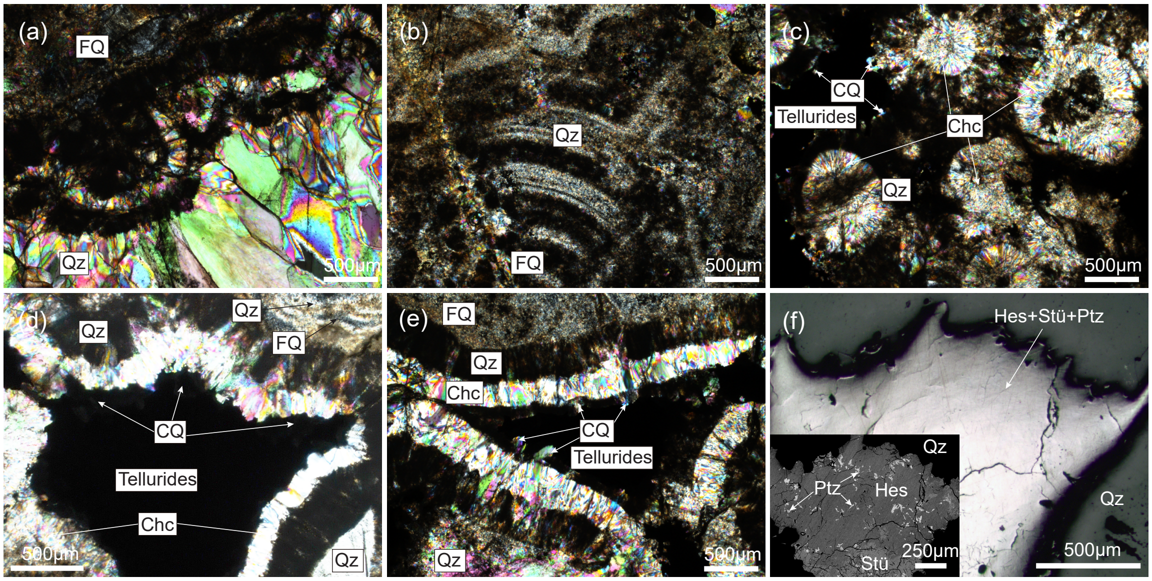

Fig. 6

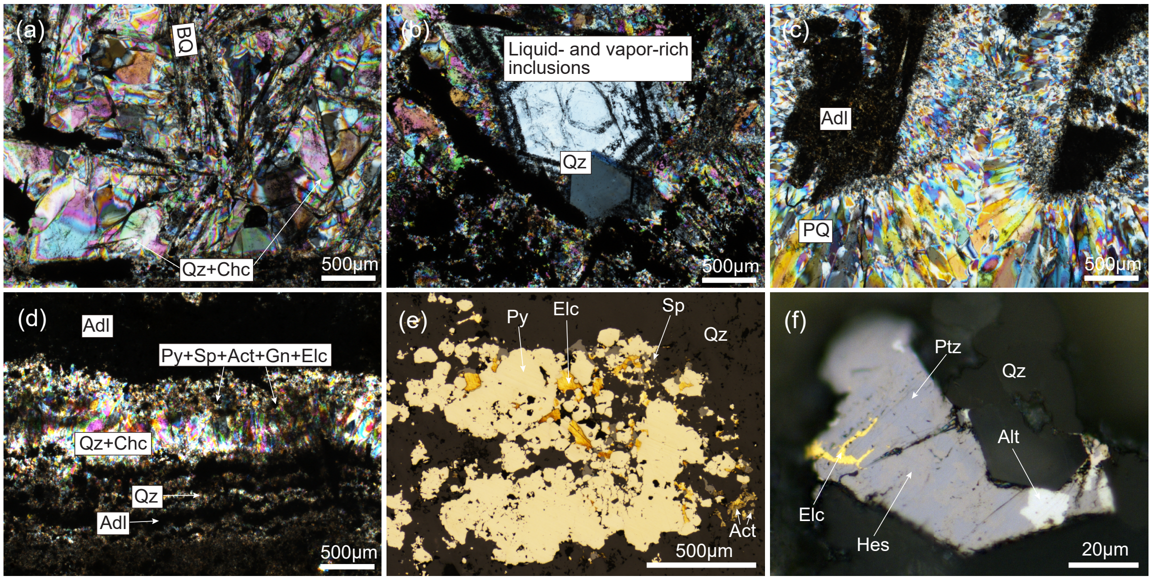
(a)
BQ
Qz+Chc
500μm
(b)
Liquid- and vapor-rich inclusions
Qz
500μm
(c)
Adl
PQ
500μm
(d)
Adl
Py+Sp+Act+Gn+Elc
Qz+Chc
Qz
Adl
500μm
(e)
Py
Elc
Sp
Qz
Act
500μm
(f)
Ptz
Qz
Alt
Elc
Hes
20μm

Fig. 7

DOI: https://doi.org/10.2138/am-2021-7825. http://www.minsocam.org/

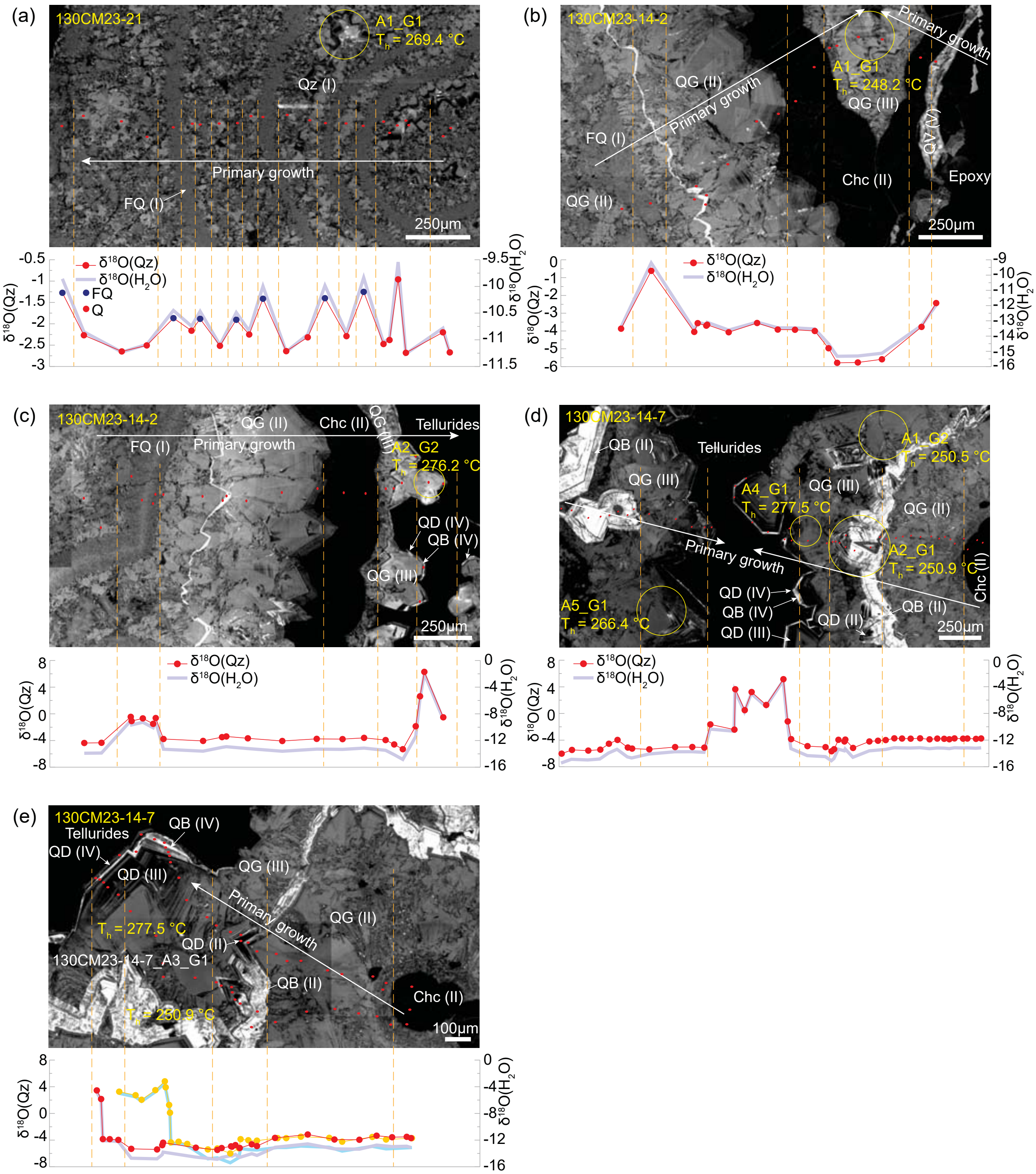

Fig. 8

DOI: https://doi.org/10.2138/am-2021-7825. http://www.minsocam.org/

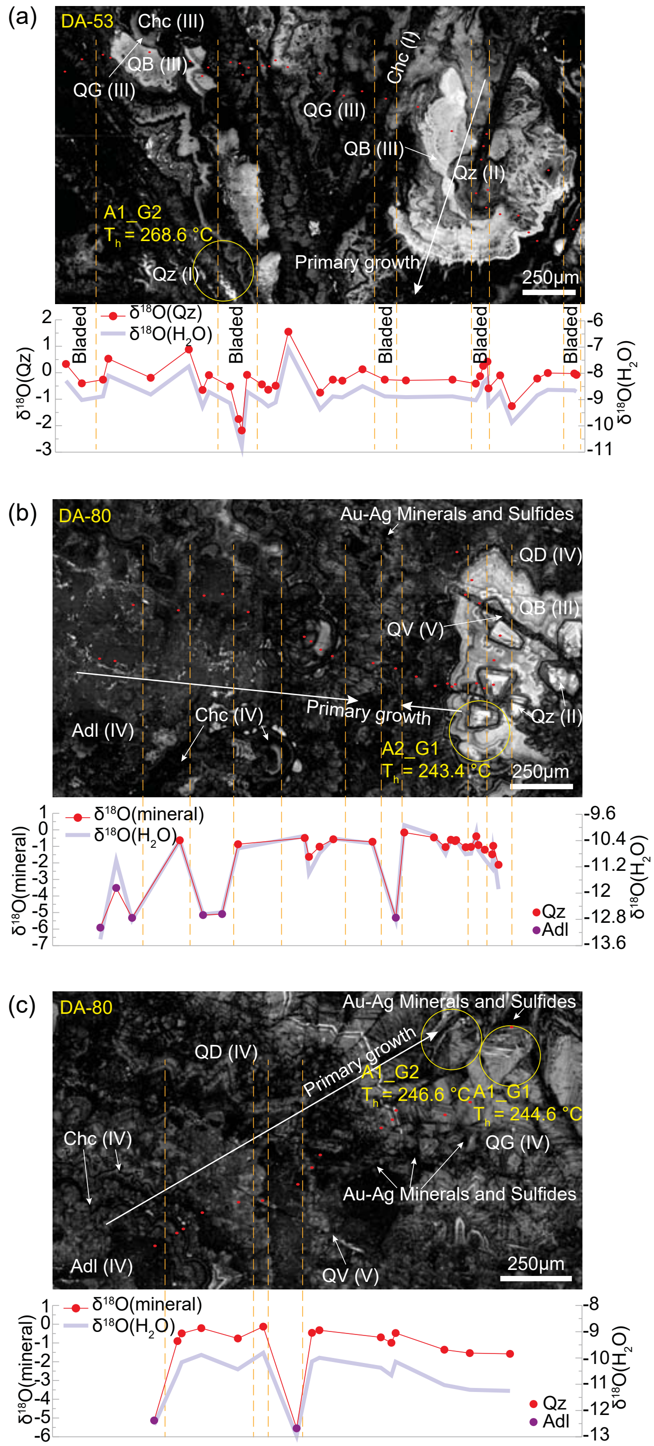

Fig. 9

This is the peer-reviewed, final accepted version for American Mineralogist, published by the Mineralogical Society of America.
The published version is subject to change. Cite as Authors (Year) Title. American Mineralogist, in press.
DOI: https://doi.org/10.2138/am-2021-7825. http://www.minsocam.org/

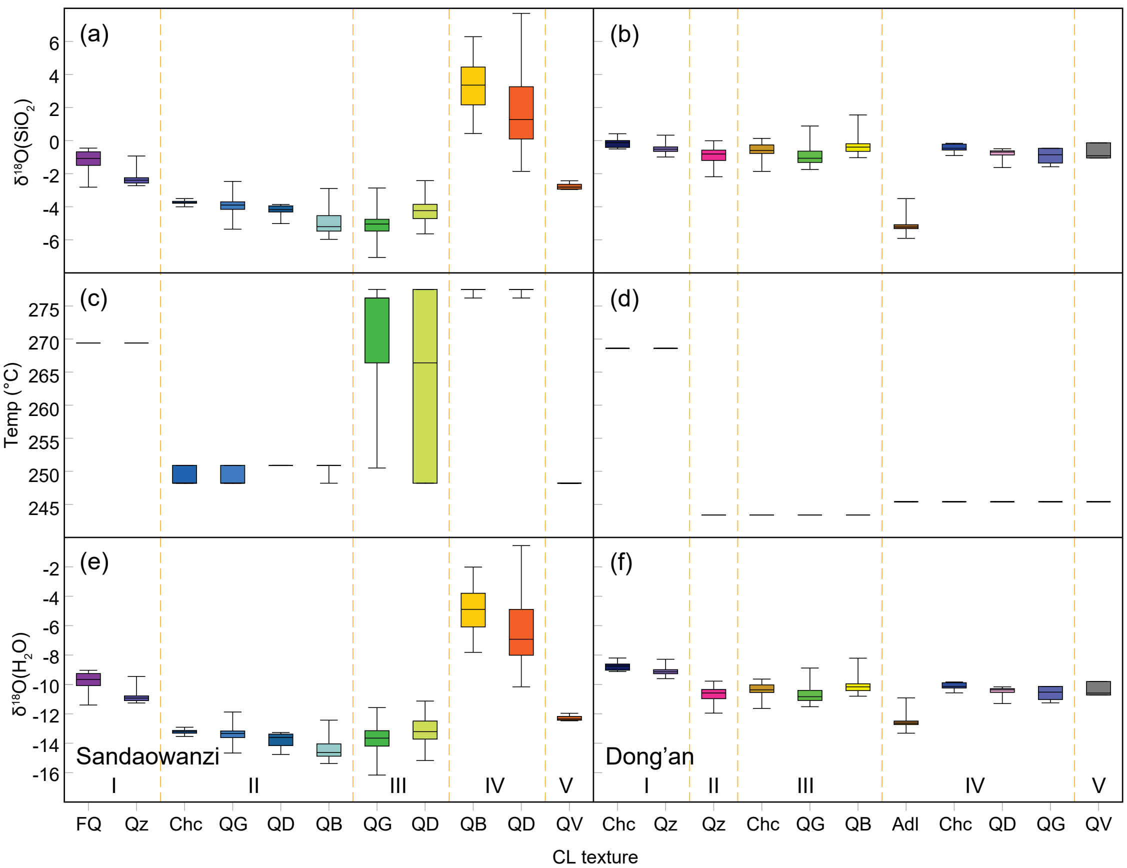

Fig. 10

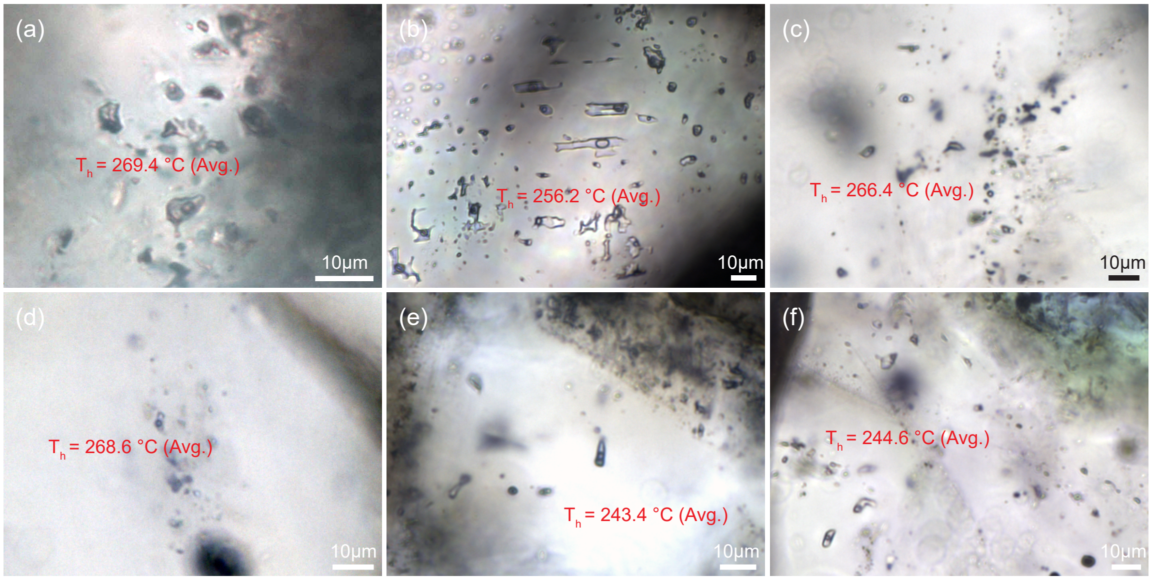
(a)
T_h = 269.4 °C (Avg.)
10μm
(b)
T_h = 256.2 °C (Avg.)
10μm
(c)
T_h = 266.4 °C (Avg.)
10μm
(d)
T_h = 268.6 °C (Avg.)
10μm
(e)
T_h = 243.4 °C (Avg.)
10μm
(f)
T_h = 244.6 °C (Avg.)
10μm

Fig. 11

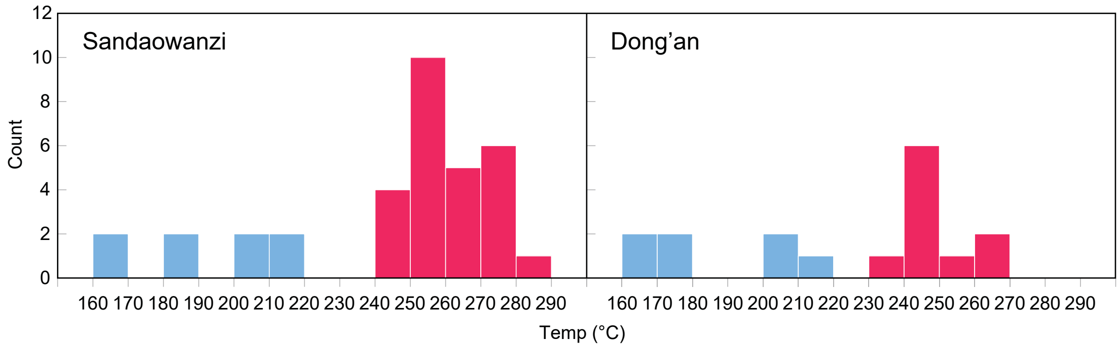
Sandaowanzi
Dong'an
Count
0
2
4
6
8
10
12
160 170 180 190 200 210 220 230 240 250 260 270 280 290
160 170 180 190 200 210 220 230 240 250 260 270 280 290
Temp (°C)

Fig. 12

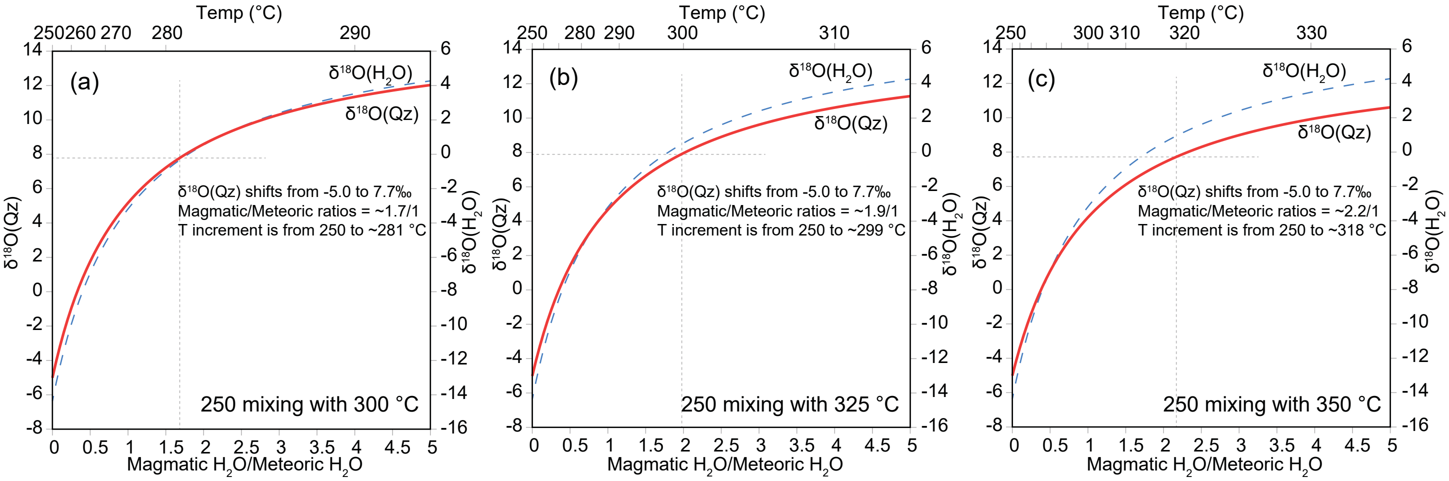
(a)
Temp (°C)
δ18O(H2O)
δ18O(Qz)
δ18O(Qz) shifts from -5.0 to 7.7‰
Magmatic/Meteoric ratios = ~1.7/1
T increment is from 250 to ~281 °C
250 mixing with 300 °C
Magmatic H2O/Meteoric H2O
(b)
δ18O(Qz) shifts from -5.0 to 7.7‰
Magmatic/Meteoric ratios = ~1.9/1
T increment is from 250 to ~299 °C
250 mixing with 325 °C
(c)
δ18O(Qz) shifts from -5.0 to 7.7‰
Magmatic/Meteoric ratios = ~2.2/1
T increment is from 250 to ~318 °C
250 mixing with 350 °C

Fig. 13